Revision 1

New insights into the crystal chemistry of sauconite (Zn-smectite) from the Skorpion zinc deposit (Namibia) via a multi-methodological approach

Emanuela Schingaro[1*], Gennaro Ventruti[1], Doriana Vinci[1], Giuseppina Balassone[2], Nicola Mondillo[2], Fernando Nieto[3], Maria Lacalamita[1], Matteo Leoni[4,5]

[1]Dipartimento di Scienze della Terra e Geoambientali, Università degli Studi di Bari Aldo Moro, Via Orabona 4, I-70125, Bari, Italy

[2]Dipartimento di Scienze della Terra dell'Ambiente e delle Risorse, Università "Federico II", Complesso Universitario Monte S. Angelo, Via Cintia, I-80126, Napoli, Italy

[3]Departamento de Mineralogía y Petrología, IACT, Universidad de Granada-CSIC, Av. Fuentenueva s/n, 18002, Granada, Spain

[4]Saudi Aramco Research and Development Center, P.O. Box 5000, 31311, Dhahran, Saudi Arabia

[5]Dipartimento di Ingegneria Civile, Ambientale e Meccanica, Università di Trento, Via Mesiano, 77, Trento, 38123, Italy

*Corresponding author: Emanuela Schingaro, e-mail: emanuela.schingaro@uniba.it

RUNNING TITLE: New insights into the crystal chemistry of sauconite

ABSTRACT

A multi-methodical characterization of a sauconite (Zn-bearing trioctahedral smectite) specimen from the Skorpion ore deposit (Namibia) was obtained by combining X-ray powder diffraction (XRPD), Cation Exchange Capacity (CEC) analysis, Differential Thermal Analysis (DTA), Thermogravimetry (TG), Fourier Transform Infrared spectroscopy (FTIR) and Transmission Electron Microscopy (TEM-HRTEM-AEM). The X-ray diffraction powder pattern exhibits the typical features of turbostratic stacking disorder with symmetrical basal *00l* reflections and long-tailed *hk*- bands, confirmed also by TEM observations. Besides sauconite, the sample also contains minor amounts of kaolinite, dioctahedral smectite and quartz. CEC analysis provides a total of Ca (~69%), Mg (~26%), Na (~4%) and K (0.7%) exchangeable cations. Therefore, Zn is located exclusively within the octahedral site of sauconite. TG analysis provides a total mass loss of about 17% in the studied sample. Three endothermic peaks can be observed in the DTA curve, associated to dehydration and dehydroxylation of the material. An exothermic peak at 820°C is also present as a consequence of dissociation and recrystallization phenomena. The infrared spectrum shows the typical Zn_3OH stretching signature at 3648 cm^{-1}, whereas, in the OH/H_2O stretching region two bands at 3585 and 3440 cm^{-1} can be associated to stretching vibrations of the inner hydration sphere of the interlayer cations and to absorbed H_2O stretching vibration, respectively. Diagnostic bands of kaolinite impurity at ~3698 and 3620 cm^{-1} are also found, whereas 2:1 dioctahedral layer silicates may contribute to the 3585 and 3620 cm^{-1} bands. Finally, using the one layer supercell approach implemented in the BGMN software, a satisfactory XRPD profile fitting model for the Skorpion sauconite was obtained. The findings have implications not only for economic geology/recovery of critical metals but, more generally, in the field of the environmental sciences.

Keywords: sauconite, nonsulfide ore deposits, Skorpion (Namibia), CEC, XRPD profile modeling, thermal analysis, FTIR, TEM

INTRODUCTION

Sauconite, a Zn-bearing trioctahedral smectite, is an ore mineral in nonsulfide Zn-Pb deposits, which typically form by weathering of precursor Zn-sulfide mineralizations under different tectonic contexts and climates, but can be also genetically related to hydrothermal fluids circulation (Large 2001; Hitzman et al. 2003; Boni and Mondillo 2015). Sauconite is commonly associated to other Zn-minerals, like smithsonite, hydrozincite, hemimorphite, willemite and various 10 Å- and 7 Å-spaced phyllosilicates (Emselle et al. 2005; Mondillo et al. 2015; Buatier et al. 2016; Arfè et al. 2017b; Balassone et al. 2017). With a content up to 50 wt.% Zn oxide, sauconite can be an accessory mineral, like in various occurrences in Belgium, Ireland, Morocco, Peru (i.e. Balassone et al. 2008, 2020; Coppola et al. 2008; Boni et al. 2009a, 2009b; Mondillo et al. 2014, 2015; Buatier et al. 2016; Choulet et al. 2016; Arfè et al. 2017a, 2017b). In some other notable cases e.g., in Yanque, Peru (Mondillo et al. 2014) and Skorpion Namibia (Borg et al. 2003; Kärner 2006; Arfè et al. 2017a; Balassone et al. 2017) it can be an important source of metal. Relatively recent developments in procedures combining leaching, solvent extraction and electrowinning, and their application to Zn smelting, have made sauconite amenable for economic Zn recovery, creating an interest in ore deposits dominated by these Zn-silicates (Gnoinski 2007; de Wet and Singleton 2008; Abkhoshk et al. 2014). However, Zn-clays also represent low-cost materials being synthesized at lower temperature compared to smectites with other transition metals (Carniato et al. 2020 and references therein). Smectite group minerals have a 2:1 layered structure made of negatively charged octahedral and tetrahedral sheets, with water molecules and partly exchangeable cations located in the interlayer space (Brigatti et al. 2006). These features, as well as the small

particle size (<100 nm), the large specific surface area (>10 m^2/g) and the presence of surface functional groups (i.e. ≡Al-OH and ≡Si-OH) are responsible for the uptake of various metal ions (i.e. Churchman et al. 2006; Balderman et al. 2019, and references therein), making such materials suitable for industrial pollution and wastewater treatment, as well as for chemical barrier applications (among the vast literature on these issues, see for instance Churchman et al. 2006; Pascua et al. 2010; Sasaki et al. 2016; Steudel et al. 2017, and references therein; Mercurio et al. 2018, and references therein). For example, Zn can be incorporated as Zn^{2+} cations in the interlayer space of swelling structures (i.e. Bradbury and Baeyens 1999; Churakov and Dähn 2012). The potential role of clay minerals in relation to the origin of life, for their role of strong adsorbents of polar organic molecules that can facilitate abiogenesis, has been also recently investigated by Zhou et al. 2017, and references therein), who studied in particular the behavior of Zn clay (sauconite).

Even though several studies have been published on the chemical characterization of natural sauconite from different deposits (i.e. Ross 1946; Faust 1951; Newman and Brown 1987; Kärner 2006; Coppola et al. 2008; Kaufhold et al. 2015; Mondillo et al. 2015; Buatier et al. 2016; Choulet et al. 2016; Balassone et al. 2017, 2020) and of synthetic sauconite (i.e. Decarreau et al. 1987; Higashi et al. 2002; Yokoyama et al. 2006; Petit et al. 2008; Pascua et al. 2010; Zhou et al. 2017), only few of them (Faust 1951; Coppola et al. 2008; Kaufhold et al. 2015; Choulet et al. 2016) report some structural features of this Zn-smectite. This lack is essentially due to the intrinsic complexity of sauconite, caused by the occurrence of stacking disorder, common in layered minerals (Lanson 2011), as well as by the variable extent of cation substitutions, different coordination and positional disorder of interlayer cations, variable number of water molecules and different interlayer water configurations. Furthermore, to the authors' knowledge, very few studies exist on the cation exchange behavior of natural sauconite. Specifically, Mitra and Sindhu (1971) investigated the cation exchange capacity of sauconite treated with H-resin and aged in water using the sauconite

from Arkansas in Ross (1946) as starting material, whereas more recently a multianalytical study (comprising CEC experiments) was carried out by Choulet et al. (2016) on Moroccan sauconite (discussed below).

In the present study, a sauconite specimen from the Skorpion ore deposit (Namibia) has been investigated using complementary techniques, i.e. a combination of X-Ray Powder Diffraction (XRPD), thermal analysis, Fourier Transform Infrared (FTIR) as well as Cation Exchange Capacity (CEC) measurements, to provide a sound mineralogical characterization as well as new insights into the species from a structural point of view. The final aim is to shed new light on such Zn trioctahedral smectite, starting from the case of study of a natural Zn-clay, in the context of practical implications not only for the economic geology and ore processing but also, on a broader level, for many fields of materials, environmental and life sciences.

MATERIALS AND METHODS

Sample occurrence and description

The Skorpion ore deposit (Vedanta Ltd.) is located ca. 40 km north of the Orange River and about 15 km north-northwest of Rosh Pinahmine in the southern most Namib Desert (Namibia), and represents the 8th largest Zn mine in the world (Boni and Mondillo 2015). The Zn mineralization is hosted in Neoproterozoic rocks of mixed volcano-sedimentary origin, described in detail in Borg et al. (2003) and Kärner (2006). In the Skorpion ore deposit, sauconite mainly occurs in metasilicoclastic rocks (mainly arkoses), as coatings of intergranular spaces and voids formed through the breakdown or dissolution of detrital feldspar and mica, or also by replacement of earlier deposited hemimorphite and smithsonite (Kärner 2006). Sauconite predominates over the other Zn-oxidized minerals (e.g. smithsonite, hydrozincite, hemimorphite, tarbuttite). The formation process of the Skorpion Zn-bearing supergene minerals started, probably, at the end of Cretaceous, after the

exhumation, weathering and oxidation of precursor sulfides (sphalerite, pyrite, minor chalcopyrite and galena), hosted in late Proterozoic felsic metavolcanic and metasilicic clastic rocks (Borg et al. 2003; Kärner 2006). The metal-bearing (Zn-dominated) fluids percolating through the rocks were able to dissolve some of their detrital silicic clastic components, i.e. mainly detrital feldspars and micas as well as the calcite cement, which provided Si and Al, together with alkaline ions, for sauconite formation. The mineral-water reactions of the hydrolysis processes must have buffered the pH of the supergene fluids, since two strong bases were produced, namely NaOH and KOH (Sherman 2001). These bases contributed to the buffering/neutralization of the acid meteoric fluids, which migrated through the Skorpion meta-arkoses. Thus, the supergene fluids became less acidic during the progressive leaching of feldspars from the Late Proterozoic rocks. This neutralization process played a significant role in the formation of the supergene nonsulfide zinc orebody, rising Eh and pH to moderate conditions, most favorable for the precipitation of the supergene zinc-bearing minerals, among which sauconite. In particular, sauconite formation requires Eh-pH conditions similar to hemimorphite and smithsonite (i.e. neutral to weak alkaline oxidizing conditions), although it can be also stable under weak acid conditions (Kärner 2006, and references therein). Based on a recent study (Arfè et al. 2017a), the stable isotope data of supergene carbonates suggest that the nonsulfide mineral assemblage formed at an average temperature of 17°C, either during the first (Late Cretaceous-Paleocene), or the last humid climatic stage (early-middle Miocene).

Starting from very heterogeneous materials and in order to select a sauconite-rich fraction as pure as possible and suitable for a full crystal chemical and structural characterization, the rock sample labelled SK8 was considered the best candidate among the Skorpion sample suite, being particularly rich in sauconite (Balassone et al. 2017). In the bulk sample, Balassone et al. (2017) also found minor amounts of Fe-oxy-hydroxides, quartz and muscovite. For the present study, white

fragments of the SK8 rock sample were selected and coarsely ground in agate mortar; any possible contaminant discernible at the stereomicroscope scale was carefully removed by hand-picking. Then, the purity of sample was checked by X-ray powder diffraction on a small fraction of powdered sample.

Cation exchange capacity

The cation exchange capacity was measured with 0.01 M Cu-triethylenetetramine (Cu-TETA) after Meier and Kahr (1999). A detailed description of this method is given in Steudel et al. (2009). About ~100 mg of SK8 powdered sample was divided in two aliquots in order to check for the reproducibility of the analysis. The results are reported in Table 1.

X-ray Powder Diffraction

Preliminary XRPD screening of selected fractions of sample SK8 was performed by a Seifert MZVI-GE system, with ID3003 generator, equipped with Ni-filtered Cukα radiation generated at 40 kV and 30 mA. The scanning area covered a 3-70° 2θ range with a step scan 0.02° and an exposure time 5 sec/step. Qualitative analysis was carried out with the RayfleX (GE) software package based on the ICDD PDF-2 database.

The XRPD patterns for structural investigations of sauconite were collected using a PANalytical Empyrean diffractometer equipped with a 1.8 kW CuKα ceramic X-ray tube, a Real Time Multiple Strip (RTMS) PIXcel3D detector. Analytical conditions were: 40 mA and 40 kV, 2θ range from 4 to 70°, a scanning speed of 0.026°/s, counting time 360 s per step. The incident beam pathway included a 0.125° divergence slit, a 0.25° antiscattering slit and 0.02 rad Soller slits, whereas a Ni filter, 0.02 rad Soller slits and an antiscatter blade (7.5 mm) were mounted in the diffracted beam pathway. Random mount was obtained by side loading the powder in a flat sample holder. Oriented

mounts were prepared following consolidated procedures (see for instance Moore and Reynolds 1997). The sample heated at 900°C after TGA-DTA analysis (see below) was also investigated by XRPD. X-ray patterns were preliminarily analyzed using the X'Pert High Score 3.0e software which includes the ICSD database, whereas the structural characterization was carried out by means of the Rietveld refinement software BGMN (Bergmann et al. 1998) using the new graphical user interface Profex (Doebelin and Kleeberg 2015). The results of XRPD investigation are reported on Figures 2, 3, 4 and 9.

Thermal analysis

Simultaneous differential thermal, thermogravimetric and derivative thermogravimetric analysis (DTA/TG/DTG) was carried out using a Toshiba STA7200RV analyzer. The measurements were performed on about 20 mg of SK8 sample placed in an alumina crucible and heated from room temperature up to 900°C at a rate of 10°C/min in a nitrogen flow (60 mL/min).

The TG-DTA-DTG curves of the SK8 sauconite are shown in the Figure 5 whereas the observed peaks and the phenomena which may occur at each temperature for the studied and literature sauconite are listed in Table 2.

Infrared analysis

Fourier transform infrared measurements were acquired using a Nicolet 380 FTIR spectrometer equipped with an EverGlo source, a KBr beamsplitter and a deuterated triglycine sulfate (DTGS) detector. FTIR spectra were collected in transmission mode on pellets of 13 mm discs with a sample-to-dried KBr weight ratio of l:200. The nominal resolution was 4 cm^{-1} and 128 scans over the range 450–4000 cm^{-1} were averaged for each sample and background. The complete FTIR spectrum of sauconite is shown in Figure 6. The results of fitting of the OH/H_2O stretching region

are displayed in Figure 7 whereas measured band positions and assignments for the studied and literature sauconite are summarized in Table 3.

TEM-HRTEM and AEM

Textural vs. structural studies down to nanoscale on sample SK8 were carried out by TEM-HRTEM at the Centro de Instrumentacion Cientifica of Granada (CIC, Spain). Copper rings were attached to representative selected areas of thin sections prepared with Canada balsam and ion-thinned using a Fischione Model 1050 ion mill, and then carbon coated. Ion milling was performed at 4 kV and ±10°, until the first hole and ±7° during 20 min for final cleaning. The HRTEM analysis was carried out by means of a Titan G2 80 300 TEM with XFEG emission gun, spherical aberration corrector and HAADF detector, working at 300 kV, with a resolution of 0.8 Å in the TEM mode and 2 Å in the STEM mode. EDX spectra for qualitative identification of minerals and chemical maps were obtained using the Super-X system; quantitative X-ray microanalysis performed in an analytical electron microscope (AEM) equipped with an EDS module allowed to obtain elemental composition of nanometric region of mineralogical samples when operating with TEM-HRTEM (Abad et al. 2003). Mineral standards were measured using the same protocol as for the sample evaluation, to obtain K-factors for the transformation of intensity ratios to concentration ratios according to Cliff and Lorimer (1975).

RESULTS AND DISCUSSION

Chemical features

The chemical composition of the studied SK8 sauconite was recently obtained by AEM and ICP-OES methods (Balassone et al. 2017). The ICP-OES analyses gave a composition with all the values inside the range of those obtained by AEM, expressed in wt.% oxides, namely: SiO_2 37.93,

This is the peer-reviewed, final accepted version for American Mineralogist, published by the Mineralogical Society of America.
The published version is subject to change. Cite as Authors (Year) Title. American Mineralogist, in press.
DOI: https://doi.org/10.2138/am-2020-7460. http://www.minsocam.org/

Al_2O_3 6.23, FeO 0.01, MgO 0.40, CaO 1.55, Na_2O 0.02, K_2O 0.03, ZnO 38.75, LOI 15.11. The ICP-OES results also discarded Na as a significant interlayer cation, solving the problem of its determination by EDX technique. The average structural formula, calculated from the analyses presented by Balassone et al. (2017) on the basis of 22 negative charges, i.e., $O_{10}(OH)_2$ is:

$$Na_{0.004}K_{0.004}Ca_{0.16}(Zn_{2.87}Al_{0.12}Mg_{0.03}Fe^{2+}_{0.01})_{\Sigma=3.03}(Si_{3.50}Al_{0.50})_{\Sigma=4.00}O_{10}(OH)_2 \cdot nH_2O.$$

The CEC determination allowed to modify that composition (see Table 1), determining a higher amount of exchangeable Mg (~26%), besides Ca (~69%), Na (~4%) and K (0.7%). The sum of exchangeable cations, when expressed as cmol+/kg, amounts to 80.2, which is in good agreement with the measured CEC values (80.9 and 80.2 cmol+/kg for the two powder aliquots, Table 1). It is also in the range of CEC values (~50-180 cmol+/kg) typically found for smectite (Schiffman and Southard 1996; Ikhsan et al. 2005; Krupskaya et al. 2017). The amount of Zn cations in the studied exchanging solution was, as expected, < 1%. These results confirm 1) the scarcity of Na and K, 2) the role of Mg as interlayer cation, 3) the location of Zn in the octahedral layer. The resulting modified crystal chemical formula for the investigated Skorpion sauconite is:

$$Na_{0.004}K_{0.004}Ca_{0.16}Mg_{0.03}(Zn_{2.87}Al_{0.12}Fe^{2+}_{0.01})_{\Sigma=3.00}(Si_{3.5}Al_{0.5})_{\Sigma=4.00}O_{10}(OH)_2 \cdot nH_2O.$$

In the ternary plot of Figure 1, the chemical composition of the studied sample is illustrated in comparison to those of the selected literature sauconite specimen. Note that the SK8 sauconite plots toward the Zn-rich region of the diagram, whereas Ross (1946) and Faust (1951) specimen are more scattered due to the high variability of the Zn content (from 1.5 to 2.9 atoms per formula unit).

XRPD characterization

The XRPD pattern measured from the random mount is shown in Figure 2. The sauconite identification was carried out taking into account all peaks in the 4-70° 2θ range. Peak positions are

similar to those found in the literature for other sauconite specimen (Faust 1951; Higashi et al. 2002; Kaufhold et al. 2015). At this stage of the investigation, initial cell parameters of SK8, to be used in subsequent refinements (see below), were provided by Check Cell program of the Crysfire suite (Shirley 1999). The results are: $a \sim 5.27$Å, $b \sim 9.24$ Å, $c \sim 15.10$ Å and $\beta \sim 99.3°$, that can be compared with those (a = 5.34 Å, b = 9.32 Å, c = 15.8 Å and β = 95°) provided by only one reference in the literature, i.e. Ross (1946) cited in Brigatti et al. (2011). All major peaks of the X-ray diffraction pattern of the random mount were indexed on the basis of the above lattice parameters. The position of the first order 001 reflection indicates a basal spacing of 14.99 Å, compatible with an interlayer space hosting 2-water planes, similarly to what recently found by Kaufhold et al. (2015). The 001 peak is weakly asymmetric at the low angle side. This feature is likely due to the inhomogeneous distribution of substitutions in both tetrahedral and octahedral sites, resulting in the coexistence of different hydrated layers in the same crystal structure at a given relative humidity (see review in Ferrage 2016). Asymmetric *hk0* reflections (e.g. 130 at 2.66 Å, 150 at 1.74 Å, see the inset of Figure 2) are also visible, whereas *hkl* reflections with $l \neq 0$ and h or $k \neq 0$ are extinct. These are typical features of diffraction pattern of clay minerals affected by turbostratic disorder along the c^* axis (Drits et al. 1984; Moore and Reynolds 1997).

Along with the characteristic reflections of sauconite, some peaks (not assigned in the inset of Figure 2) are indicative of small amount of impurity, likely represented by K-feldspar, quartz, muscovite, kaolinite and dioctahedral smectite.

The occurrence of the diagnostic 060 reflection at 1.54 Å confirms the trioctahedral nature of sauconite whereas the broad reflection near 1.50 Å is consistent with the presence of disordered kaolinite.

X-ray diffraction measurements on oriented mounts after air drying (AD), ethylene-glycolation (EG) and thermal treatments were carried out following the procedure in Reynolds (1980) and

Moore and Reynolds (1997). The comparison of the AD and EG pattern in Figure 3 clearly evidences a shift of the 001 peak from ~14.9 Å in the AD pattern to 16.8 Å in the EG sauconite, as expected for this mineral (see also Higashi et al. 2002; Yokoyama et al. 2006; Coppola et al. 2008; Kaufhold et al. 2015; Choulet et al. 2016). Moreover, the 001 peak is centered at 15.1 Å in the pattern collected after heating at 400°C, whereas it shifts to 9.6 Å when the sauconite is heated at 550°C as a consequence of the shrinking of the smectite along the stacking direction (Jackson 1979; Higashi et al. 2002). The sauconite 002 peak at 7.47 Å is asymmetric in the AD pattern because of the presence of the basal reflection of kaolinite (at 7.16 Å), which is barely visible in the pattern from the random mount. This peak shifts to 8.40 Å in the EG pattern, whereas the 001 reflection of kaolinite remains unchanged (see inset of Figure 3). The pattern collected after heating at 400°C, instead, resembles the AD one although all peaks appears more broadened. Finally, in the pattern at 550°C, the 001 peak of kaolinite disappears.

Figure 4 illustrates the pattern of the sample after heating at 900°C. The characteristic peaks of residual sauconite, cristobalite, willemite (α-Zn_2SiO_4) were identified (see the next section).

Thermal analysis

The curves from TGA-DTA-DTG experiments are shown in Figure 5 and the relevant results compared with literature data are listed in Table 2. The thermogravimetric and differential analysis exhibits several weight losses, which evidence the occurrence of several reactions including dehydration and dehydroxylation. From DTA curve, broad signals are observed at 93, 190, 370, 500, 550-740 and 820°C. The signals at 93 and 190°C are, respectively, due to water that is readily removable through drying or heating, as well as water that is more strongly bound, totaling ~11.8% weight loss. This two-step dehydration is in agreement with previous works (Kaufhold et al. 2015) and consistent with the two-layer hydration of the sauconite studied here, testified by the (001) d-

spacing from XRPD analysis (Moore and Reynolds 1997). The broad band around 93°C could be due to the loss of half of the water molecules linked to the interlayer cations, accounting for the change from bi-layer to mono-layer states, as defined by Ferrage et al. (2007a, 2007b). The peak around 190ºC could be associated with removal of the remaining layer of water molecules, that is, to the complete dehydration of the interlayer. This interpretation is in agreement with the conclusions of Poinsignon et al. (1982), Bray et al. (1998) and Bray and Redfern (1999). The latter authors find on smectite a two step behavior at temperatures very close to those of our sample whereas Ferrage et al. (2007a, 2007b) indicate slightly lower temperatures for the transition to a one-layer state.

The weak endothermic signals in the range 370-500°C are of uncertain attribution, because they can originate from a broad range of effects, for instance decarboxylation of organic matter, occurrence of hydroxides, LHD minerals, dehydroxylation of 1:1 (Hedley et al. 2007; Drits and Zviagina 2009; Földvári 2011, see Table 2). Drits and Zviagina (2009) indicate dehydroxylation temperatures <600°C for illite and smectite layers but admit interference, in interpretation of thermal analysis, due to kaolinite and/or chlorite impurities. However, in our sample these signals are associated to about 1% weight loss.

The weight loss in the 550-740°C range is due to dehydroxylation of sauconite and accounts for about 3% of the total weight loss. Therefore, assuming that all mass loss is due to the release of water from sauconite and that the amount of other phases is negligible, the thermal analysis provides a total mass loss of about 17% which accounts for ~4 H_2O groups in the studied sauconite.

Finally, the exothermic peak at 820°C may be associated to the breakdown of sauconite and crystallization of new phases (see also Faust 1951; Higashi et al. 2002; Petit et al. 2008; Kaufhold et al. 2015, and Table 2). There is no complete agreement in the literature about the phases formed upon heating. Faust (1951) found that, heating sauconite at 866°C, just above the dissociation point,

firstly γ-Zn_2SiO_4 and subsequently β-Zn_2SiO_4 and gahnite are formed. The same author, heating above 1000°C, obtained a mixture of willemite (α-Zn_2SiO_4), cristobalite and gahnite. Taylor (1962) got insights on the stability of β-Zn_2SiO_4 by studying the dehydration of hemimorphite. He found that hemimorphite transforms, at 700°C directly to β-Zn_2SiO_4 and then, at < 960°C, to willemite. In more recent thermal studies of sauconite (Higashi et al. 2002; Petit et al. 2008; Kaufhold et al. 2015), recrystallization products after sauconite heating were not analyzed. As already stated in the XRPD characterization paragraph above, sauconite is still present in the 900°C pattern, together with willemite and cristobalite. Gahnite and clinopyroxene occurrence (previously reported by Faust 1951) are uncertain since the relevant peaks fall underneath those of the main phases.

FTIR results

The OH/H_2O absorption occurs in the region extending from 4000 to 3000 cm^{-1} whereas the Si-O and Zn-O vibration bands are observed in the region from 1500 to 450 cm^{-1} (Figure 6). The OH stretching region of the studied sauconite evidences a broad absorption band extending from 3860 to 3000 cm^{-1}, caused by remarkable band overlapping. Seven bands have been used to fit the region, as shown in Figure 7. The narrow peak at 3648 cm^{-1} (band B) is associated to Zn_3OH stretching vibrations, as observed in the Silver Coin sauconite (Kaufhold et al. 2015) and for the synthetic samples in Higashi et al. (2002), Yokoyama et al. (2006) and Petit et al. (2008). The band at 3551 cm^{-1} (band E) may be associated to combination of Fe-, and Zn-OH stretching vibration as also proposed for the Silver Coin sauconite in Kaufold et al. (2015), see Table 3. Based on studies of montmorillonite exchanged with different interlayer cations under variable moisture environments (Bishop et al. 1994), the band at 3585 cm^{-1} (band D) may be attributed to water of the inner hydration sphere of the interlayer cations whereas the band at 3440 cm^{-1} (band F) may be due to absorbed H_2O stretching vibration (Russel and Farmer 1964). The band at 1633 cm^{-1} is associated to

This is the peer-reviewed, final accepted version for American Mineralogist, published by the Mineralogical Society of America.
The published version is subject to change. Cite as Authors (Year) Title. American Mineralogist, in press.
DOI: https://doi.org/10.2138/am-2020-7460. http://www.minsocam.org/

H_2O bending vibrations, whereas the 3230 cm^{-1} (band G) band corresponds to the H_2O bending overtone (Eisenberg and Kauzmann 1969).

Finally, the bands at ~3698 and 3620 cm^{-1} (bands A and C, respectively) are due to AlAlOH stretching vibrations of kaolinite (Balan et al. 2001; Madejová and Komadel 2001; Kaufhold et al. 2015). However, bands C and D could also be affected by the contribution of other dioctahedral phases (Zviagina et al. 2004; Castellini et al. 2017). These evidences are also in agreement with the XRD analysis (see above).

TEM-HRTEM

TEM-HRTEM shows compact clay packages (CCP, i.e. straight and almost iso-oriented packets with a length up to several micrometers and a thickness below ~1 μm; Mondillo et al. 2015; Balassone et al. 2017) and porous clay aggregates (PCA, i.e. very fine-grained packets with sizes below ~ 400 nm; Mondillo et al. 2015; Balassone et al. 2017), as illustrated in Figure 8. The SAED pattern of the CCP sauconite region is shown in the inset of Figure 8a, and corresponds to a partially collapsed smectite with an interlayer spacing of ~12 Å, which typically occurs as a consequence of TEM vacuum and/or electron irradiation. Smectite was characterized by (001) SAED patterns with streaks parallel to c*. Non-00l reflections are ill-defined, non-periodic, and diffuse parallel to c*. In Figure 8b and 8d the transition area between CCP and PCA is shown. High resolution images were obtained (Figure 8c). The smectite is characterized by discontinuous, wavy (001) fringes with spacings from 12 Å to 14 Å, with variation in interplanar spacing and contrast. Even the spacing varies through the layers. The d values depend on the degree of dehydration and of layer collapse caused by interaction with the electron beam on the TEM or ion-mill vacuums. There are abundant layer terminations and the boundaries between packets are diffuse. The various sub-packets, considering these as areas constituting a coherent crystalline domain, show an

anastomosing relationship to each other, with frequent layer terminations at low-angle contacts with the neighbor sub-packet. The chemical mapping of the area of Figure 8e confirms the AEM data (Balassone et al. 2017) and the results reported in the section "Chemical features" above and shows that the specimen is fairly homogeneous at the TEM scale.

XRPD profile modeling

To date no suitable structural model is available for sauconite, because this clay mineral is found in nature always turbostratically disordered (inset Figure 8a). As already noted in the section XRPD characterization above, the peculiar shape of sauconite diffraction peaks (Figure 2) is indicative of the occurrence of this kind of disorder. In turbostratic stacking disorder, individual layers in the crystal structures are statistically rotated and translated with respect to each other (Drits and Tchoubar 1990), thus breaking the electron density periodicity along the stacking direction. Lattice fringe images and electron diffraction data (Figures 8c and 8a) confirm this microstructural feature with a view in the direct space, which explains the characteristics of the reciprocal space information here obtained. Different methodological approaches can be used to model the powder diffraction pattern of turbostratically-disordered layered structures.

The DIFFaX+ code (Leoni et al. 2004) is able to model the pattern of faulted layered materials using the recursive algorithm of Treacy et al. (1991). The latter code was used by Viani et al. (2002) to simulate the diffraction pattern of a Ca-montmorillonite, but their final model of disorder was rather that of a highly faulted structure with random shifts along ± **b**/3 and – **a**/3, with 75% of defect density than that of a truly turbostratically disordered strucure, with 100% of defect density. Random translations, which dominate the turbostratic effect, can be simulated by using a supercell containing several layers translated by random amounts relative to each other. This approach was successfully developed by Ufer et al. (2004) and handled in the BGMN software (Bergmann et al.

1998) through a language interpreter. Subsequently it was applied to improve quantitative phase analyses of smectites (Ufer et al. 2008) and to refine some structural parameters (Ufer et al. 2012; Wang et al. 2018).

In this work, diffraction pattern of the of turbostratically disordered Skorpion sauconite has been fitted using the one-layer supercell approach developed by Ufer et al. (2004).

The starting structure model of sauconite was prepared by modifying the Tsipursky and Drits (1984) de-hydrated K-saturated smectite with monoclinic space group *C*2 (their model 2). The interlayer space was increased to 15 Å to simulate a bi-hydrated Ca-smectite. The species and occupancies of interlayer, octahedral and tetrahedral cations in the supercell model were fixed from the calculated sauconite formula, considering only Ca as the interlayer cation. The geometry of TOT layer was adapted to that of a trioctahedral one, by varying the coordinates in order to obtain reasonable Zn-O bond distances (Sham and Wu 1999). A rigid-body model of the interlayer cations (Ca) octahedrally coordinated to water molecules was used and the cation polyhedron was allowed to rotate to guarantee that the two water planes be parallel to the *ab*-plane, as suggested by specific literature (Slade et al. 1985; Beyer and von Reichenbach 2002) The refinement yielded <Ca-Ow> = 2.51(3) Å. A supercell was used, stacking 30 layers along the c_0 direction, a size sufficiently large to contain all relevant stacking correlations and to generate smooth *hk* peaks by superposition of different orders of *hkl* reflections. An additional broadening parameter which accounts for the dependence of the *l* index on the peak width was also introduced in the modeling (Ufer et al. 2004). The supercell was filled with just one layer of 15 Å thickness. Then, 00*l* reflections are generated from the 15 Å subcell and their intensity was modified to account for proper cell filling. The pattern was modeled in the 4-70° 2θ range. The best fit model was achieved by also refining lattice parameters (*a*, *b* and *c*), size and microstrain broadening parameters to match the measured sauconite pattern. For sauconite anisotropic preferential orientation was also refined, that in BGMN

is implemented by using spherical harmonics (Bergmann et al. 2001). The impurity phases, i.e. kaolinite, dioctahedral smectite and quartz were also included in the refinement. The crystal structure data for the impurity phases were taken from: Tsipursky and Drits (1984) cis-vacant model, with d_{001} modified to ~ 15 Å and disorder model after Ufer et al. 2004 for smectite; Bish and von Dreele (1979) for kaolinite model and Ufer et al. 2015 for kaolinite disorder modeling (their Kga-2 sample); D'Amour et al. 1979 for α-quartz. The chemistry of the diocahedral smectite was constrained to that of beidellite in Balassone et al. 2017. For the impurity phases only cell parameters and peak broadening parameters were refined as well as the phases scale factors. The simulated pattern reproduces the main features present in the experimental pattern (Figure 9). The main misfits are at 2θ = 5.90, 24.5 and 45°. The misfit at 2θ = 5.90° corresponding to 001 sauconite reflection is likely due to the not homogenous hydration at the interlayer (Ferrage et al. 2005; Kaufhold et al. 2011; Dazas et al. 2013; Ferrage 2016; Wang et al. 2018; Vinci et al. 2020). The other two misfits have 3.63 and 2.01 Å d-spacings respectively, showing a good match with the 1*M* muscovite of Soboleva et al. (1975). However, attempts to introduce this phase as well as K-feldspar into the fitting were unsuccessful. Other contributions to the misfit, such as the occurrence of smectite with mixed 1W/2W interlayer hydration cannot be ruled out. The final fitting converged to R_{wp} = 5.50 %, R_{pb} = 7.42 %, R = 5.52 %, R_{wp} = 7.48 %, R_{exp} = 2.84 %, χ^2 = 7.54. The refined values of the lattice constants are: a = 5.3430(5) Å, b = 9.2419(5) Å, c = 15.3696(2) Å. Note that the expected $a = b/\sqrt{3}$ condition for trioctahedral layer (Brindley 1980) is fulfilled within the experimental error. The phase fractions are: sauconite 81.7(7) %, kaolinite 7.8(4) %, dioctahedral smectite 10.4(5) %, and traces of quartz, confirming that sauconite is the major component in the mixture. The overall quality of the fitting can be considered satisfactory, considering that we are dealing with a mixture consisting mostly of disordered phases, where parameter refinement has to proceed with caution, to facilitate convergence and to get stable refinements with structurally

meaningful parameters. Similar procedures are commonly adopted when the Rietveld technique is applied to such complex patterns also for quantitative phase analyses (see for instance Lutterotti et al. 2010; Ufer et al. 2012, 2015).

IMPLICATIONS

This paper contributes to the improvement of the knowledge on a class of Zn-bearing minerals, whose properties are of relevance not only to economic geologists, but also to exploration geochemists and environment scientists. The Zn availability has indeed an impact not only at a global industrial level, to develop proper treatments and extraction processes for both primary ore and secondary materials (see, for example, Cole and Sole 2003; Boni et al. 2009a; Choulet et al. 2016), but also in terms of bioavailability considering that Zn is a micronutrient or a toxin to plant and animal life (McPhail et al. 2003). The above issues, among others, benefit from a deeper understanding of the ore mineral types and of the crystal chemical behavior of valuable metals, such as Zn. The employed multi-methodical approach provides some crystal chemical insights of the sauconite structure, based on the octahedral sheet almost entirely occupied by Zn ions and an interlayer region occupied by alkali cations surrounded by two water planes parallel to the octahedral-tetrahedral layers. Consistently, CEC results show that Ca and Mg ions, in small amounts, are hosted in the interlayer sites, whereas Zn ions are located within the octahedral site of sauconite. Therefore, an adsorption mechanism of the Zn^{2+} cations at the clay surface or fixing of the Zn^{2+} cations in the interlayer is negligible or lacking (see also Choulet et al. 2016).

On considering that the natural sample at hand is not pure and consists of a number of disordered phases, the findings provided here can be considered a further contribution demonstrating that the approach developed in Ufer et al. (2004) can be successfully applied to increasingly challenging real cases, provided that cross-checking with independent techniques is

also used. In addition, the present work can have implications for a better comprehension of the hydration properties of trioctahedral smectites. The latter topic, related to the assessment of the interlayer cations and the interlayer water organization is widely recognized as crucial in determining the swelling/collapsing behavior in smectite with high impact both in the field of civil engineering and soil science and, more generally, in the environmental sciences, since the smectite hydration properties, often characterized by heterogeneity at different scales, may affect the fate/transfer properties of pollutants in natural media (see for instance Ferrage 2016 and references therein).

ACKNOWLEDGMENTS

The XRPD laboratory at the Dipartimento di Scienze della Terra and Geoambientali, University of Bari "Aldo Moro", was funded by Potenziamento Strutturale PONa3_00369 "Laboratorio per lo Sviluppo Integrato delle Scienze e delle TEcnologie dei Materiali Avanzati e per dispositivi innovativi (SISTEMA)". The XRPD facility at the DiSTAR, University "Federico II" Napoli, is acknowledged. The authors acknowledge Annett Steudel and Katja Emmerich for CEC measurement at the Competence Center for Material Moisture, University of Karlshrue, Germany. GB and NM thank Maria Boni, invaluable scientific guide who promoted the study of the economic geology of worldwide nonsulfide ore deposits, and G. Arfè who firstly characterized the Skorpion samples and for continuous help and fruitful discussions. This work was partly supported by DiSTAR fund 2017 (University of Naples Federico II, Italy) granted to G. Balassone, as well as by the research projects PGC2018-094573-B-100 from the Spanish Government and the Research Group RNM-179 of the Junta de Andalucía granted to F. Nieto. Two anonymous referees are thanked for insightful comments that helped to improve the quality of the manuscript.

REFERENCES CITED

Abad, I., Gutiérrez-Alonso, G., Nieto, F., Gertner, I., Becker, A., and Cabero, A. (2003) The structure and the phyllosilicates (chemistry, crystallinity and texture) of Talas Ala-Tau (Tien Shan, Kyrgyz Republic): comparison with more recent subduction complexes. Tectonophysics, 365, 1-4, 103-127.

Abkhoshk, E., Jorjani, E., Al-Harahsheh, M.S., Rashchi, F., and Naazeri, M. (2014) Review of the hydrometallurgical processing of non-sulfide zinc ores. Hydrometallurgy, 149, 153-167.

Arfè, G., Boni, M., Balassone, G., Mondillo, N., Hinder G., and Joachimski, M. (2017a) New C-O isotopic data on supergene minerals from the Skorpion and Rosh Pinah ore deposits (Namibia): genetic and palaeoclimatic constraints. Journal of African Earth Sciences, 126,148-158.

Arfé, G., Mondillo, N., Balassone, G., Boni, M., Cappelletti, P., and Di Palma, T. (2017b) Identification of Zn-bearing micas and clays from the Cristal and Mina Grande zinc deposits (Bongará Province, Amazonas Region, Northern Peru). Minerals, 7(11),214.

Arfè, G., Mondillo, N., Boni, M., Balassone, G., Joachimski, M., Mormone, A., and Di Palma, T. (2017c) The karst-hosted Mina Grande nonsulfide zinc deposit, Bongará district (Amazonas region, Peru). Economic Geology, 112, 1089-1110.

Balan, E., Saitta, A.M., Mauri, F., and Calas, G. (2001) First-principles modeling of the infrared spectrum of kaolinite. American Mineralogist, 86, 1321-1330.

Balassone, G., Rossi, M., Boni, M., Stanley, G., and McDermott, P. (2008) Mineralogical and geochemical characterization of nonsulfide Zn–Pb mineralization at Silvermines and Galmoy (Irish Midlands). Ore Geology Reviews, 33, 168-186.

Balassone, G., Nieto, F., Arfè, G., Boni, M., and Mondillo, N. (2017) Zn-clay minerals in the Skorpion Zn nonsulfide deposit (Namibia): Identification and genetic clues revealed by HRTEM and AEM study. Applied Clay Science, 150, 309-322.

Balassone, G., Scognamiglio, V., Nieto, F., Mondillo, N. Boni, M., Cappelletti, P., and Arfè, G. (2020) The nature of Zn-phyllosilicates in the nonsulfide Mina Grande and Cristal zinc deposits (Bongará district, northern Peru): the TEM-HRTEM and AEM perspective. American Mineralogist, in press.

Balderman, A., Landler, A., Mittermayr, F., Letofsky-Papst, I., Steind, F., Galan, I., and Dietzel, M. (2019) Removal of heavy metals (Co, Cr, and Zn) during calcium–aluminium–silicate–hydrate and trioctahedral smectite formation. Journal of Materials Science, 54, 9331-9351.

Bergmann, J., Friedel, P., and Kleeberg, R. (1998) BGMN - a new fundamental parameter based Rietveld program for laboratory X-ray sources, its use in quantitative analysis and structure investigations. Commission on Powder Diffraction Newsletter, 20, 5-8.

Bergmann, J., Monecke, T., and Kleeberg, R. (2001) Alternative algorithm for the correction of preferred orientation in Rietveld analysis. Journal of Applied Crystallography, 34, 16-19.

Beyer, J., and von Reichenbach, H. G. (1998) Dehydration and rehydration of vermiculites: IV. Arrangements of interlayer components in the 1.43 nm and 1.38 nm hydrates of Mg-vermiculite. Zeitschrift für Physikalische Chemie, 207, 67-82.

Bish, D.L., and Von Dreele, R.B. (1989) Rietveld refinement of non-hydrogen atomic positions in kaolinite. Clays and Clay Minerals, 37, 289–296.

Bishop, J.L., Pieters, C.M., and Edwards, J.O. (1994) Infrared spectroscopic analyses on the nature of water in montmorillonite. Clays and Clay Minerals, 42(6), 702-716.

Boni, M., and Mondillo, N. (2015) The "Calamines" and the "Others": the great family of supergene nonsulfide zinc ores. Ore Geology Reviews, 67, 208-233.

Boni, M., Schmidt, P.R., DeWet, J.R., Singleton, J.D., Balassone, G., and Mondillo, N. (2009a) Mineralogical signature of nonsulfide zinc ores at Accha (Peru): a key for recovery. International Journal of Mineral Processing, 93, 267-277.

Boni, M., Balassone, G., Arseneau, V., and Schmidt, P. (2009b) The nonsulfide zinc deposit at Accha (Southern Peru): geological and mineralogical characterization. Economic Geology, 104, 267-289.

Borg, G., Kärner, K., Buxton, M., Armstrong, R., and van der Merwe, S.W. (2003) Geology of the Skorpion supergene zinc deposit, southern Namibia. Economic Geology, 98(4), 749-771.

Bradbury, M.H., and Baeyens, B. (1999) Modelling the sorption of Zn and Ni on Ca-montmorillonite. Geochimica and Cosmochimica Acta, 63, 325-336.

Bray, H.J., Redfern S.A.T., and Clark, S.M. (1998) The kinetics of dehydration in Ca-montmorillonite: an *in situ* X-ray diffraction study. Mineralogical Magazine, 62(5), 647-656.

Brigatti, M.F., Galan, E., and Theng, B.K.G. (2006) Structure and mineralogy of clay minerals. In F. Bergaya, B.K.G. Theng, and G. Lagaly, Eds., Handbook of Clay Science, Developments in Clay Science, 1, p. 19-86. Elsevier, Amsterdam.

Brigatti, M.F., Malferrari, D., Laurora, A., and Elmi, C. (2011) Structure and mineralogy of layer silicates: recent perspectives and new trends. In M.F. and A. Mottana, Eds., Layered mineral structures and their Application in Advanced Technologies, EMU notes in Mineralogy, 11, p. 1-71. The Mineralogical Society of Great Britain and Ireland.

Brindley, G.W. (1980) Order-disorder in clay mineral structures. In G.W. Brindley and G. Brown, Eds., Crystal structures of clay minerals and their X-ray identification, 2, p. 125-195. Mineralogical Society of Great Britain and Ireland.

Buatier, M., Choulet, F., Petit, S., Chassagnon, R., and Vennemann, T. (2016) Nature and origin of natural Zn clay minerals from the BouArhous Zn ore deposit: Evidence from electron

microscopy (SEM-TEM) and stable isotope compositions (H and O). Applied Clay Science, 132, 377-390.

Carniato, F., Gatti, G., and Bisio, C. (2020) An overview of the recent synthesis and functionalization methods of saponite clay. New Journal of Chemistry, DOI:10.1039/D0NJ00253D

Castellini, E., Malferrari, D., Bernini, F., Brigatti, M.F., Castro, G.F., Medici, L., Mucci, A. and Borsari, M. (2017) Baseline studies of the clay minerals society source clay montmorillonite STx-1b. Clays and Clay Minerals, 65, 4, 220-233.

Choulet, F., Buatier, M., Barbanson, L., Guégan, R., and Ennaciri, A. (2016) Zinc-rich clays in supergene non-sulfide zinc deposits. Mineral Deposita, 51, 467-490.

Churakov, S.V., and Dähn, R. (2012) Zinc adsorption on clays inferred from atomistic simulations and EXAFS spectroscopy. Environmental Science & Technology, 46, 5713-5719.

Churchman, J., Gates, W., Yuan, G., and Theng, B.K. (2006) Clays and clay minerals for pollution control. In F. Bergaya, B.K.G. Theng and G. Lagaly, Eds., Handbook of Clay Science, Developments in Clay Science, 1, p. 625-675. Elsevier, Amsterdam.

Cliff, G., and Lorimer, G.W. (1975) The quantitative analysis of thin specimens. Journal of Microscopy, 103, 203-207.

Cole, P.M. and Sole, K.C. (2003) Zinc solvent extraction in the process industries. Mineral Processing & Extractive Metallurgy Review, 24, 91-137.

Coppola, V., Boni, M., Gilg, H.A., Balassone, G., and Dejonghe, L. (2008) The “Calamine” nonsulfide Zn-Pb deposits of Belgium: petrographical, mineralogical and geochemical characterization. Ore Geology Reviews, 33, 187-210.

D'Amour, H., Denner, W., and Schulz, H. (1979) Structure determination of α-quartz up to $68*10^8$ Pa. Acta Crystallographica B, 35, 550-555.

Dazas, B., Lanson, B., Breu, J., Robert, J.L., Pelletier, M., and Ferrage, E. (2013) Smectite fluorination and its impact on interlayer water content and structure: a way to fine tune the hydrophilicity of clay surfaces? Microporous and Mesoporous Materials, 181, 233-247.

de Wet, J.R., and Singleton, J.D. (2008) Development of a viable process for the recovery of zinc from oxide ores. Journal of the Southern African Institute of Mining and Metallurgy, 108(5), 253-259.

Decarreau, A., Colin, F., Herbillon A., Manceau, A., Nahon, D., Paquet, H., Trauth-Badeaud, D. andTrescases, J.J. (1987) Domain segregation in Ni-Fe-Mg-smectites. Clays and Clay Minerals, 35, 1-10.

Doebelin, N., and Kleeberg, R. (2015) Profex: A graphical user interface for the Rietveld refinement program BGMN. Journal of Applied Crystallography, 48, 1573-1580.

Drits, V.A., and Zviagina, B.B. (2009) *Trans*-vacant and *cis*-vacant 2:1 layer silicates: structural features, identification and occurrence. Clays and Clay Minerals, 57, 405-415.

Drits, V.A., and Tchoubar, C. (1990) The modelization method in the determination of the structural characteristics of some layer silicates: internal structure of the layers, nature and distribution of stacking faults. In V.A. Drits and C. Tchoubar, Eds., X-Ray Diffraction by Disordered Lamellar Structures, p. 233-303. Springer-Verlag, Berlin.

Drits, V.A., Plançon, A., Sakharov, B.A., Besson, G., Tsipurski, S.I., and Tchoubar, C. (1984) Diffraction effects calculated for structural models of K-saturated montmorillonite containing different types of defects. Clay Minerals, 19, 541-561.

Eisenberg, D., and Kauzmann, W. (1969) The structure and properties of water, 296 p. Oxford University Press, New York.

Emselle, N., McPhail, D.C., and Welch, S.A. (2005) Reliance, Flinders Ranges: mineralogy, geochemistry and zinc dispersion around a nonsulfide orebody. In C. Roach, Ed., Regolith

2005 ten tears of CRC LEME: proceedings of the CRC LEME Regional Regolith Symposia, p. 86-90. Cooperative Research Centre for Landscape Environments and Mineral Exploration, Australia.

Faust, T.G. (1951) Thermal analysis and X-ray studies of sauconite and of some zinc minerals of the same paragenetic association. American Mineralogist, 36, 795-821.

Ferrage, E. (2016) Investigation of the interlayer organization of water and ions in smectite from the combined use of diffraction experiments and molecular simulations. A review of methodology, applications and perspectives. Clays and Clay minerals, 64(4), 346-371.

Ferrage, E., Kirk, C.A., Cressey, G., and Cuadros, J. (2007a) Dehydration of Ca-montmorillonite at the crystal scale. Part I: Structure evolution. American Mineralogist, 92, 994-1006.

Ferrage, E., Kirk, C.A., Cressey, G., and Cuadros, J. (2007b) Dehydration of Ca-montmorillonite at the crystal scale. Part II. Mechanisms and kinetics. American Mineralogist, 92, 1007-1017.

Ferrage, E., Lanson, B., Sakharov, B.A., and Drits, V.A. (2005) Investigation of smectite hydration properties by modeling experimental X-ray pattern. Part I. Montmorrillonite hydration properties. American Mineralogist, 90, 1358-1374.

Földvári, M. (2011) Handbook of thermogravimetric system of minerals and its use in geological practice. 180 p. Geological Institute of Hungary.

Gnoinski, J. (2007) Skorpion Zinc: optimisation and innovation. Journal of the Southern African Institute of Mining and Metallurgy, 107, 657-662.

Hedley, C.B., Yuan, G., and Theng, B.K.G. (2007) Thermal analysis of montmorillonites modified with quaternary phosphonium and ammonium surfactants. Applied Clay Science, 35, 180-188.

Higashi, S., Miki, K., and Komarneni, S. (2002) Hydrothermal synthesis of Zn-smectites. Clays and Clay Minerals, 50, 299-305.

Hitzman, M.W., Reynolds, N.A., Sangster, D.F., Allen, C.R., and Carman, C.E. (2003) Classification, genesis, and exploration guides for nonsulfidezinc deposits. Economic Geology, 98, 685-714.

Ikhsan, J., Wells, J.D., Johnson, B.B., and Angove, M.J. (2005) Surface complexation modeling of thesorption of Zn(II) by montmorillonite. Colloids and Surface A: Physicochemical and Engineering Aspects, 252, 33-41.

Jackson, M.L. (1979) Soil chemical analysis-Advanced course: 2nd ed., Publ. by author, Dept. Soil Science, Univ. 895 p. Wisconsin, Madison, Wisconsin,

Kärner, K. (2006) The metallogenesis of the Skorpionnon-nulphidezinc deposit, Namibia, 133 p. Ph.D. thesis, Martin-Luther-Universität Halle-Wittenberg, Germany.

Kaufhold, S., Dohrmann, R., Ufer, K., Kleeberg, R., and Stanjek, H. (2011) Termination of swelling capacity of smectites by Cu_{trien} exchange. Clay Minerals, 46, 411-420.

Kaufhold, S., Färber, G., Dohrmann, R., Ufer, K., and Grathoff, G. (2015) Zn-rich smectite from the Silver Coin Mine, Nevada, USA. Clay Minerals, 50, 417-430.

Krupskaya, V.V., Zakusin, S.V., Tyupina, E.A., Dorzhieva, O.V., Zhukhlistov, A.P., Belousov, P.E., and Timofeeva, M.N. (2017) Experimental study of montmorillonite structure and transformation of its properties under treatment with inorganic acid solutions. Minerals, 7(4), 49.

Lanson, B. (2011) Modelling of X-ray diffraction profiles: Investigation of defective lamellar structure crystal chemistry. In M.F. Brigatti and A. Mottana, Eds., Bulk and Surface Structures of Layer Silicates and Oxides: Theoretical Aspects and Applications. EMU Notes in Mineralogy 11, p. 151-202. European Mineralogical Union.

Large, D. (2001) The geology of non-sulfide zinc deposits. An overview. Erzmetall: Journal for Exploration, Mining and Metallurgy, 54, 264-274.

Leoni, M., Gualtieri, A.F., and Roveri, N. (2004) Simultaneous refinement of structure and microstructure of layered materials. Journal of Applied Crystallography, 37, 166-173.

Lutterotti, L., Voltolini, M., Wenk, H-R., Bandyopadhyay, K. and Vanorio, T. (2010) Texture analysis of a turbostratically disordered Ca-montmorillonite. American Mineralogist, 95, 98-103.

Madejová, J. and Komadel, P. (2001) Baseline studies of the clay minerals society source clays: Infrared methods. Clays and Clay Minerals, 49(5), 410-432.

McPhail, D.C., Summerhayes, E., Welch, S., and Brugger, J. (2003) The geochemistry and mobility of zinc in the regolith. Advances in Regolith, 287-291.

Meier, L.P. and Kahr, G. (1999). Determination of the cation exchange capacity (CEC) of clay minerals using the complexes of copper(II) ion with triethylenetetramine and tetraethylenepentamine. Clays and Clay Minerals, 47, 386-388.

Mercurio, M., Sarkar, B., and Langella, A. (2018) Modified clay and zeolite nanocomposite materials: environmental and pharmaceutical applications, 362 p., Elsevier.

Mitra, R.P., and Sindhu, P.S. (1971) Acid character of sauconite: increase in cation exchange capacity on aging in water and the role of Zn^{2+} and Al^{3+} ions. Clays and Clay Minerals, 19, 391-397.

Mondillo, N., Boni, M., Balassone, G., and Villa, I.M. (2014) The Yanque Prospect (Peru): from polymetallic Zn-Pb mineralization to a nonsulfide deposit. Economic Geology, 109, 1735-1762.

Mondillo, N., Nieto, F., and Balassone, G. (2015) Micro- and nano-characterization of Zn-clays in nonsulfide supergene ores of southern Peru. American Mineralogist, 100, 2484-2496.

Moore, D.M., and Reynolds, R.C. (1997) X-Ray diffraction and the identification and analysis of clay minerals, 378 p. Oxford University Press, New York.

Newman, A.C.D., and Brown, G. (1987) The chemical constitution of clays. In A.C.D. Newman, Ed., Chemistry of Clays and Clay Minerals. John Wiley & Sons, New York, p.128.

Pascua, C.S., Ohnuma, M., Matsushita, Y., Tamura, K., Yamada, H., Cuadros, J., and Ye, J. (2010) Synthesis of monodisperse Zn-smectite. Applied Clay Science, 48, 55-59.

Petit, S., Righi, D., and Decarreau, A. (2008) Transformation of synthetic Zn-stevensite to Zn-talc induced by the Hofmann-Klemen effect. Clays and Clay Minerals, 56(6), 645-654.

Poinsignon, C., Yvon, J., and Mercier, R. (1992) Dehydration energy of the exchangeable cations in montmorillonite – a DTA study. Israel Journal of Chemistry, 22, 253-255.

Reynolds, R.C. (1980) Interstratified clay minerals. In G.W. Brindley and G. Brown, Eds., Crystal Structures of Clay Minerals and their X-ray Identification, 5, p. 249-303. Mineralogical Society, London.

Ross, C.S. (1946) Sauconite - a clay mineral of the Montmorillonite group. American Mineralogist, 31, 411-424.

Sasaki, Y., Shati, G.A., and Yamamoto, O. (2016) In vivo evaluation of wound healing property of zinc smectite using a rat model. Journal of Ceramic Society Japan, 124(12), 1199-1204.

Schiffman, P., and Southard, R.J. (1996) Cation exchange capacity of layer silicates and palagonitized glass in mafic volcanic rocks: a comparative study of bulk extraction and *in situ* techiniques. Clays and Clay Minerals, 44(5), 624-634.

Sham, S., and Wu, G. (1999) Zn-67 NMR study of tetrahedral and octahedral zinc sites with symmetrical oxygen, nitrogen and sulfur ligands. Canadian Journal of Chemistry, 77, 1782-1787.

Sherman, D.M. (2001) Weathering Reactions and Soil-Groundwater Chemistry. Environmental Geochemistry, University of Bristol, Unpubl. Lecture Notes 200, (2002), 11.

Shirley, R. (1999) The CRYSFIRE System for Automatic Powder Indexing: user's manual, The Lattice Press, 41 Guildford Park Avenue, Guildford, Surrey GU2 5NL, England.

Slade, P.G., Stone, P.A., and Radoslovich, E.W. (1985) Interlayer structures of the two-layer hydrates of Na- and Ca-vermiculites. Clays and Clay Minerals, 33, 51-61.

Soboleva, S.V., Zvyagin, B.B., and Sidorenko, O.V. (1975) Crystal structure refinement for 1*M* dioctahedral mica. Soviet Physics Crystallography, 20, 332-335.

Steudel, A., Weidler, P.G., Schuhmann, R., and Emmerich, K. (2009) Cation exchange reactions of vermiculite with Cu-triethylenetetramine as affected by mechanical and chemical pretreatment. Clays and Clay Minerals, 57(4), 486-493.

Steudel, A., Friedrich, F., Schuhmann, R., Ruf, F., Sohling, U., and Emmerich, K. (2017) Characterization of a fine-grained interstratification of turbostratic talc and saponite. In G. Cruciani, A. Martucci, Eds., New Insights in Stability, Structure and Properties of Porous Materials Reprinted, Minerals,7, p. 5-18.

Taylor, H.F.W. (1962) The dehydration of hemimorphite. American Mineralogist, 47, 932-944.

Treacy, M.M.J., Newsam, J., and Deem, M. (1991) A general recursion method for calculating diffracted intensities from crystals containing planar faults. In M. Lockwood, Ed., Proceeding of the Royal society A, 433, 499-520.

Tsipursky, S.I, and Drits, V.A. (1984) The distribution of octahedral cations in the 2:1 layers of dioctahedral smectites studied by oblique-texture electron diffraction. Clay Minerals, 19, 177-193.

Ufer, K., Kleeberg, R., Bergmann, J., and Dohrmann, R. (2012) Rietveld refinement of disordered illite-smectite mixed-layer structures by a recursive algorithm. II: powder-pattern refinement and quantitative phase analysis. Clays and Clay Minerals, 60, 535-552.

Ufer, K., Kleeberg, R., Bergmann, J., Curtius, H., and Dohrmann, R. (2008) Quantitative phase analysis of bentonite by the Rietveld method. Clays and Clay Minerals, 56, 272-282.

Ufer, K., Roth, G., Kleeberg, R.,Stanjek, H., Dohrmann, R.,and Bergmann, J. (2004) Description of X-ray powder pattern of turbostratically disordered layer structures with a Rietveld compatible approach. Zeitschrift für Kristallographie, 219(9), 519-527.

Ufer, K., Kleeberg, R., and Monecke, T. (2015) Quantification of stacking disordered Si-Al layer silicates by the Rietveld method: application to exploration for high-sulphidation epithermal gold deposits. Powder Diffraction, 30, S111-S118.

Viani, A., Gualtieri, A., and Artioli, G. (2002) The nature of disorder in montmorillonite by simulation of X-ray powder patterns. American Mineralogist, 87,966-975.

Vinci, D., Dazas, B., Ferrage, E., Lanson, M., Magnin, V., Findling, N., and Lanson, B. (2020) Influence of layer charge on hydration properties of synthetic octahedrally-charged Na-saturated trioctahedral swelling phyllosilicates. Applied Clay Science, 184, 105404.

Yokoyama, S., Tamura, K., Hatta, T., Nemoto, S., Watanabe, Y., and Yamada, H. (2006) Synthesis and characterization of Zn-substituted saponite (sauconite). Clay Science, 13, 75-80.

Wang, X., Ufer, K, and Kleeberg, R. (2018) Routine investigation of structural parameters of dioctahedral smectites by the Rietveld method. Applied Clay Science, 163, 257-264.

Zhou, R., Basu, K., Hartman, H., Matocha, C.J., Sears, S.K., Vali, H., and Guzman, M.I. (2017) Catalyzed synthesis of zinc clays by prebiotic central metabolites. Scientific Reports, 7(533), 1-12.

Zviagina, B. B., McCarty, D.K., Środoń, J., and Drits, V. A. (2004) Interpretation of infrared spectra of dioctahedral smectites in the region of OH-stretching vibrations. Clays and Clay Minerals, 52, 4, 399–410.

Figure captions

Figure 1. Ternary diagram after Choulet et al. (2016). 4Si: Si/4; $3R^{2+}$: $R^{2+}/3$; M^{+}: $M^{+} + 2M^{2+}$. Note that $3R^{2+}$ here is more general than in Choulet et al. (2016), who set $3R^{2+} = (Fe + Mg + Zn)/3$. Symbols: full black square indicate the SK8 sample from Balassone et al. (2017). Open symbols for literature sauconites (square: SK1 and SK3 samples from Balassone et al. (2017); circle: Choulet et al. (2016); green triangle pointing upward: Kaufhold et al. (2015); triangle pointing downward: Mondillo et al. (2015); diamond: Mondillo et al. (2014); diamond with horizontal bar inside: Boniet et al. (2009); square with horizontal bar inside: Kärner (2006); circle with horizontal bar inside: Faust (1951); red triangle pointing upward with horizontal bar inside: Ross (1946).

Figure 2. Random mount XRPD pattern of the sample SK8. The inset showsan enlargement of the 10-65° 2θ range. Sau = sauconite.

Figure 3. XRPD patterns of the air dried (AD, black line), ethylene glycol treated (EG, red line), heated at 400°C (green line), heated at 550°C (blue line) sauconite. In the inset: enlargement of the 9-40° 2θ range with the value of the d-spacing of the sauconite 002 reflection and the position of the kaolinite (K) basal reflection in the EG pattern.

Figure 4. XRPD patterns in 4-69° 2θ range of sauconite after heating at 900°C. Sau = sauconite; Crist = cristobalite; Wil = willemite.

Figure 5. TGA (blue line), DTA (black line) and DTG (red line) curves of SK8 sauconite measured in air.

Figure 6. Room temperature infrared spectrum of SK8 sauconite in the range 4000-450 cm^{-1}.

Figure 7. Results of fitting of the OH stretching region for the SK8 sauconite.

Figure 8. (a) TEM textural image of CCP sauconite SK8, with a SAED pattern of the investigated area in the inset; (b) textural image of CCP sauconite locally with a PCP character; (c) lattice fringe image of the area in the yellow frame of (b), showing small disoriented packets, locally vanishing into each other; (d) CCP textural image with the yellow frame corresponding to image (a); (e) chemical mapping the same area as in (d).

Figure 9. XRPD modeling of the Skorpion sauconite. (a) Fitting in the 4-70° 2θ range; (b) enlargement of the fitting in the 10-70° 2θ range. Data color legend: black, observed; red, calculated; green, sauconite; cyano, kaolinite; magenta, dioctahedral smectite; brown, quartz; yellow, background; blue, difference.

This is the peer-reviewed, final accepted version for American Mineralogist, published by the Mineralogical Society of America.
The published version is subject to change. Cite as Authors (Year) Title. American Mineralogist, in press.
DOI: https://doi.org/10.2138/am-2020-7460. http://www.minsocam.org/

Table 1. Values of the CEC and of the exchangeable cations (cmol+/kg) for the studied sauconite.

	Aliquot 1	**Aliquot 2**
Sample weight (g)	0.0432	0.0392
CEC	80.93	80.21
Ca	55.2	
Mg	20.7	
Na	3.3	
K	0.5	
Zn	0.5	

This is the peer-reviewed, final accepted version for American Mineralogist, published by the Mineralogical Society of America.
The published version is subject to change. Cite as Authors (Year) Title. American Mineralogist, in press.
DOI: https://doi.org/10.2138/am-2020-7460. http://www.minsocam.org/

Table 2. Data (°C) from the DTA curve of the SK8 and literature sauconite.

This study	Kaufhold et al. (2015)	Petit et al. (2008)	Higashi et al. (2002)	Faust (1951)				Phenomena
	ZnS-1 (<0.5 µm)		Synthetic sample	c-134	c-80	c-81	c-567	
100	120	63-83	90					Sauconite dehydration (absorbed H_2O)
				178	170	165	158	Sauconite dehydration (absorbed and interlayer H_2O)
190			246	289	270	273	261	Sauconite dehydration (interlayer H_2O)
						305*	353*	-
	330*							Oxydation of organic matter or effect of gibbsite
380**								Organic matter decarboxylation
				441				Sauconite dehydration (absorbed H_2O); dehydroxylation
500**	500							Kaolinite dehydroxylation.
								Oxydation of organic matter or effect of gibbsite
				582		601	569	Decomposition of halloysite
550-700	650	550-615	615	734	728	729	682	Sauconite dehydroxylation
820*	800*	765-781	770*	832*	818*	895*	836*	Breakdown of sauconite structure and recrystallization
	900*	952-968	964*	978*	940*	1029*		Breakdown of sauconite structure and recrystallization

Note: *Exothermal peak.**In the 380-500°C range, and, in general at T<600°C, contribution due to dehydroxylation of 1:1 and/or 2:1 trans vacant clay mineral may occur (see text).

This is the peer-reviewed, final accepted version for American Mineralogist, published by the Mineralogical Society of America.
The published version is subject to change. Cite as Authors (Year) Title. American Mineralogist, in press.
DOI: https://doi.org/10.2138/am-2020-7460. http://www.minsocam.org/

Table 3. Position (cm^{-1}) and assignment for the bands in the infrared spectrum of the SK8 and literature sauconite.

	This study	Kaufhold et al. (2015)	Petit et al. (2008)	Yokoyama et al. (2006)	Higashi et al. (2002)	Band assignment
Band				cm^{-1}		
A	3698	3698				**Kaolinite**
B	3648	3640	3643	3635	3641	**ZnZnZn-OH**
C	3620	3623				**AlAl-OH of kaolinite**; **2:1 dioctahedral phases**
				3600-3200		ν_3 H_2O
D	3585					**H_2O of inner sphere; 2:1 dioctahedral phases**
E	3551	3558				**FeFeZn-OH** or MgMgZn-OH or FeMgZn-OH
		3530				FeFeZn-OH or MgMgZn-OH or FeMgZn-OH or FeFe-OH MgZn-OH
F	3440	3442				**Absorbed H_2O**; Gibbsite band
		3375				Gibbsite band
G	3230					**H_2O bending overtone**
	1633			1600	1600	**Interlayer H_2O bending**

Note: Assignment for this study in bold (see text)

This is the peer-reviewed, final accepted version for American Mineralogist, published by the Mineralogical Society of America.
The published version is subject to change. Cite as Authors (Year) Title. American Mineralogist, in press.
DOI: https://doi.org/10.2138/am-2020-7460. http://www.minsocam.org/

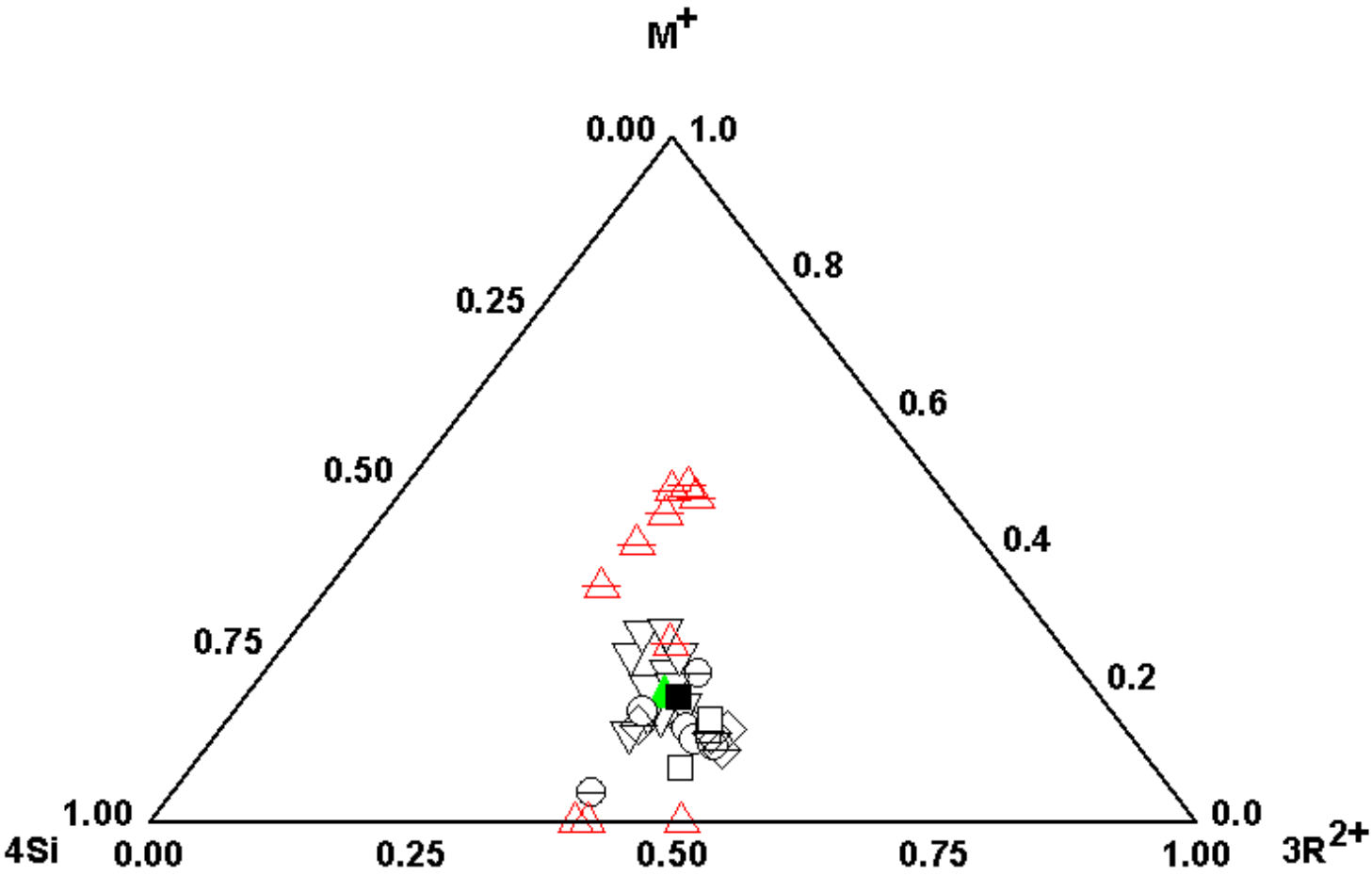

Fig. 1 Rev

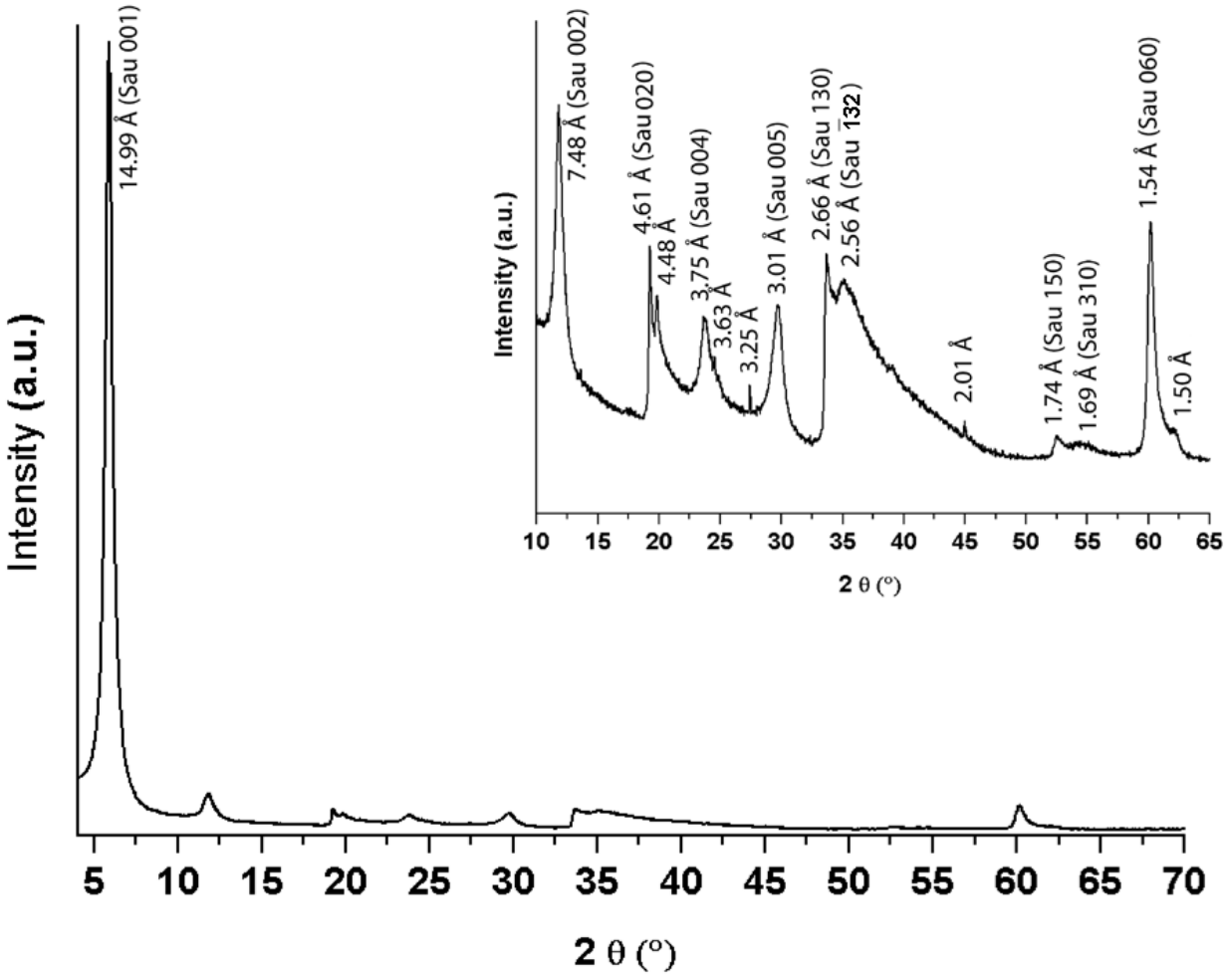

Fig. 2

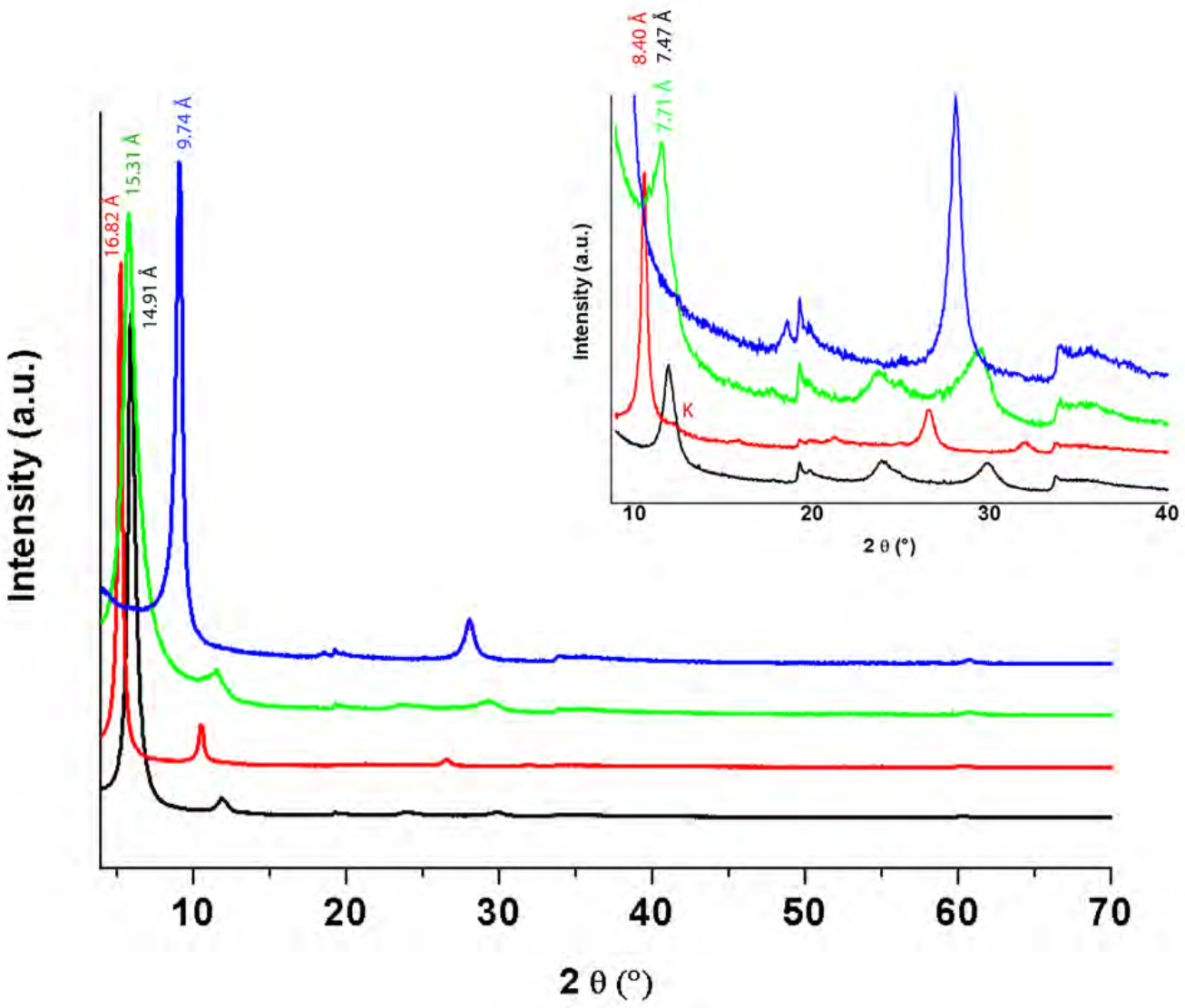

Fig. 3 Rev

This is the peer-reviewed, final accepted version for American Mineralogist, published by the Mineralogical Society of America.
The published version is subject to change. Cite as Authors (Year) Title. American Mineralogist, in press.
DOI: https://doi.org/10.2138/am-2020-7460. http://www.minsocam.org/

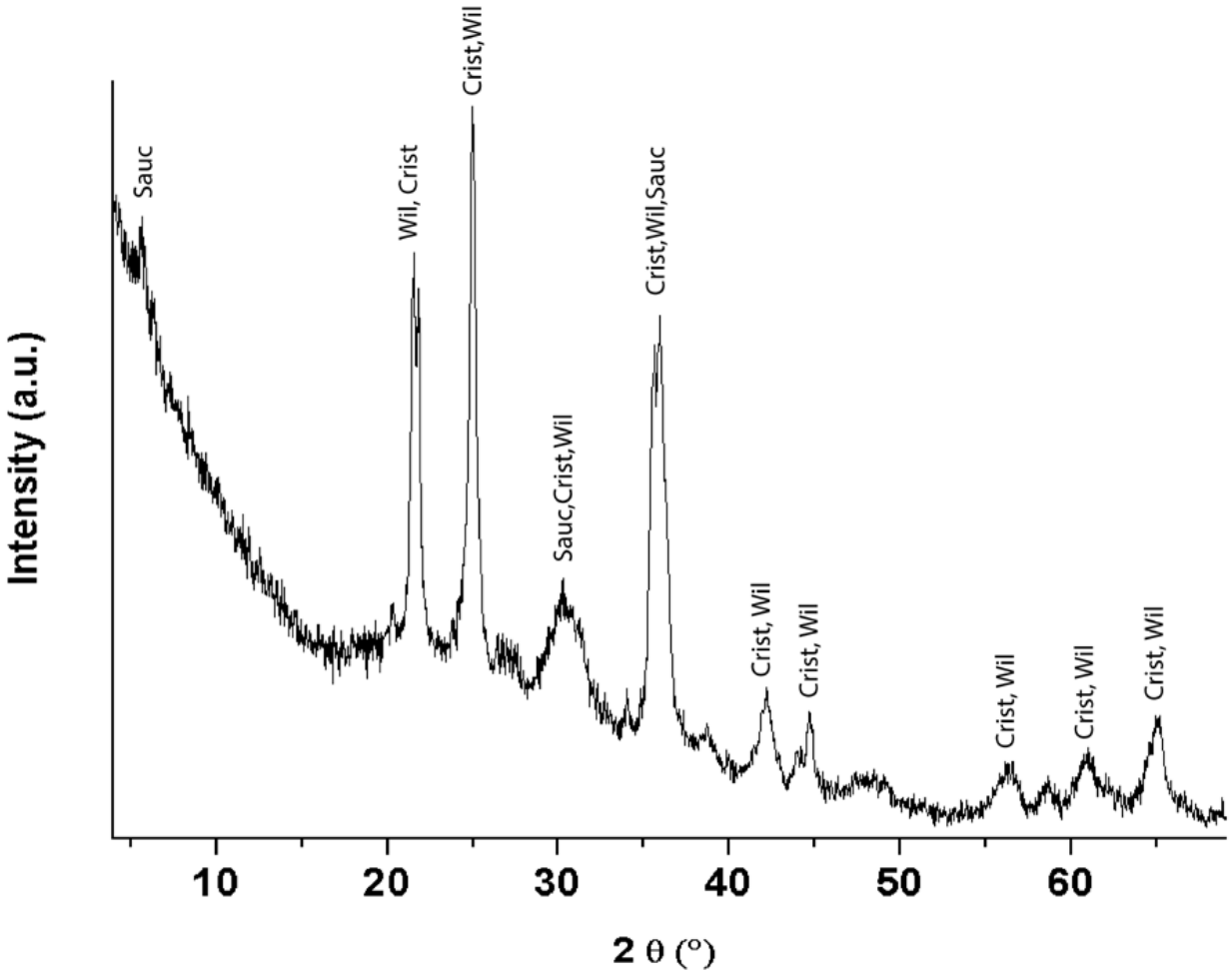

Fig. 4

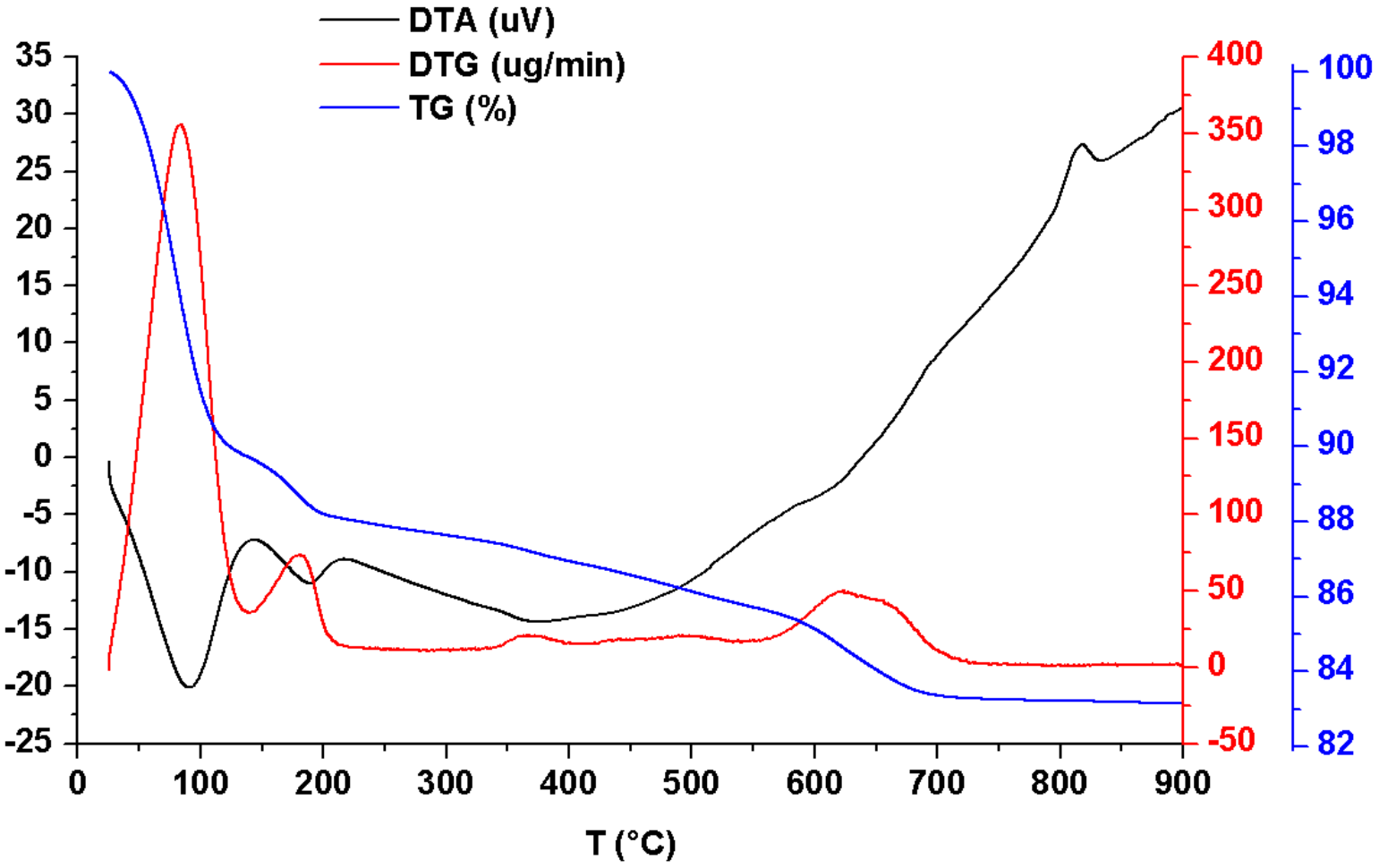

Fig. 5

This is the peer-reviewed, final accepted version for American Mineralogist, published by the Mineralogical Society of America.
The published version is subject to change. Cite as Authors (Year) Title. American Mineralogist, in press.
DOI: https://doi.org/10.2138/am-2020-7460. http://www.minsocam.org/

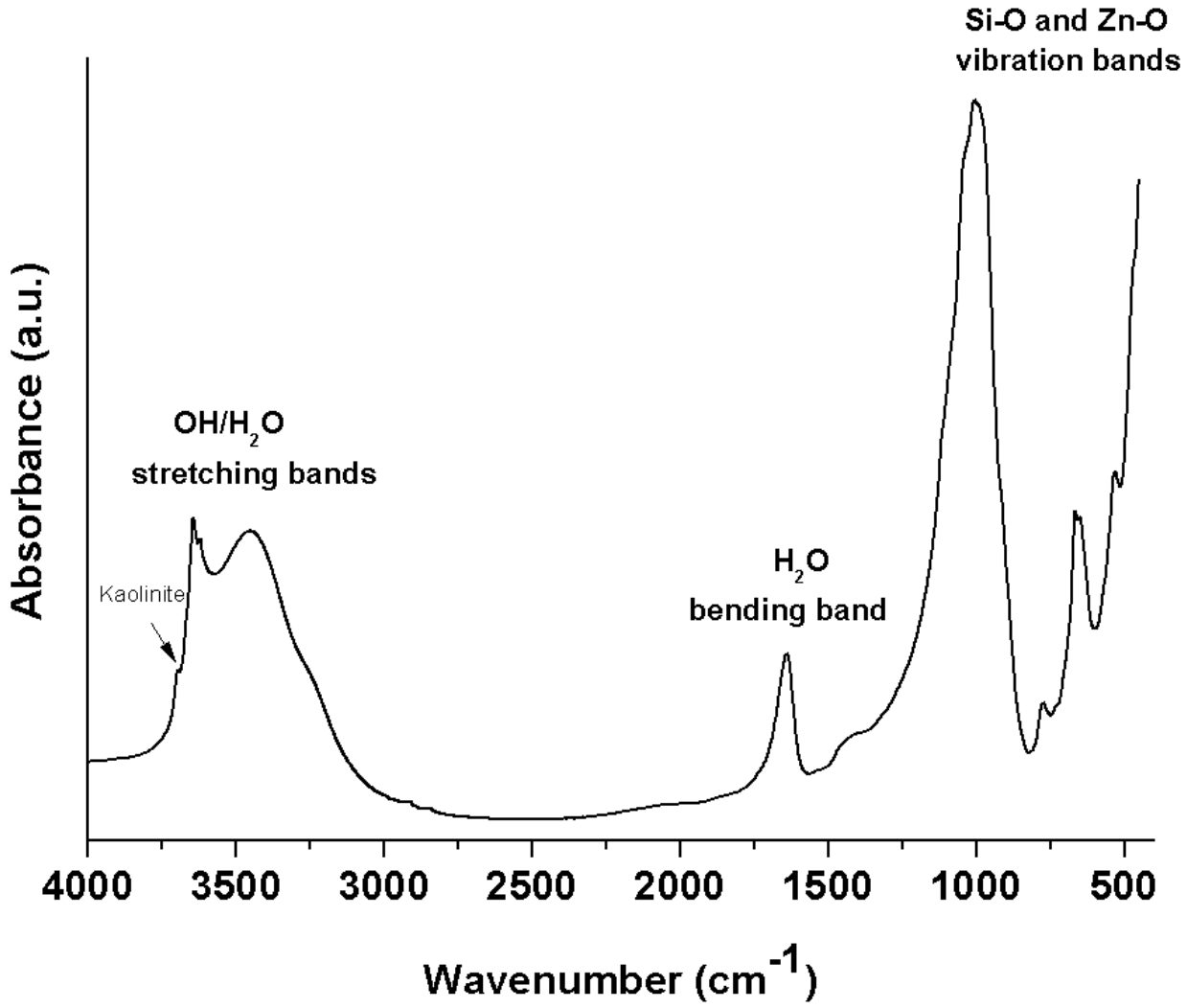

Fig. 6

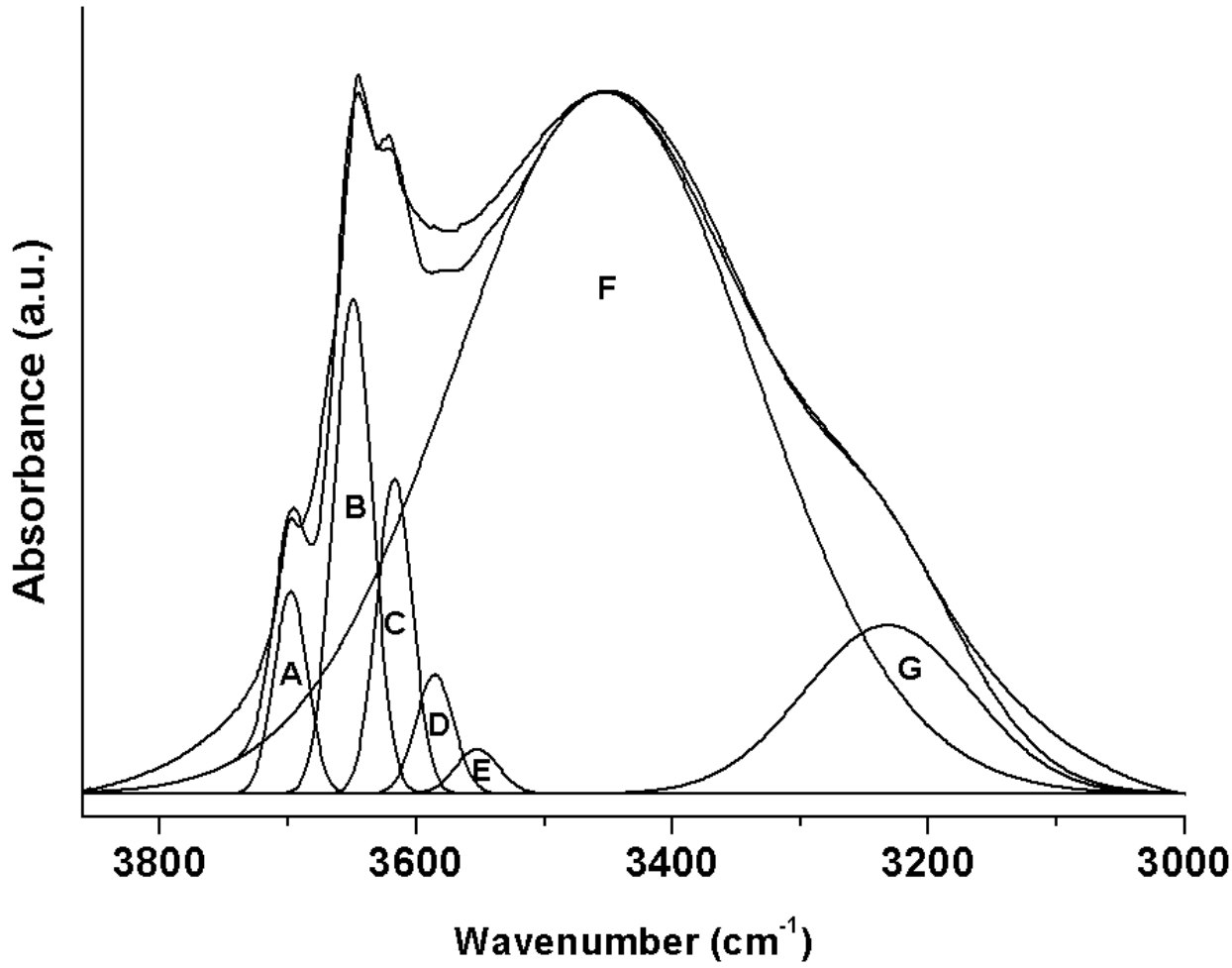

Fig. 7

This is the peer-reviewed, final accepted version for American Mineralogist, published by the Mineralogical Society of America.
The published version is subject to change. Cite as Authors (Year) Title. American Mineralogist, in press.
DOI: https://doi.org/10.2138/am-2020-7460. http://www.minsocam.org/

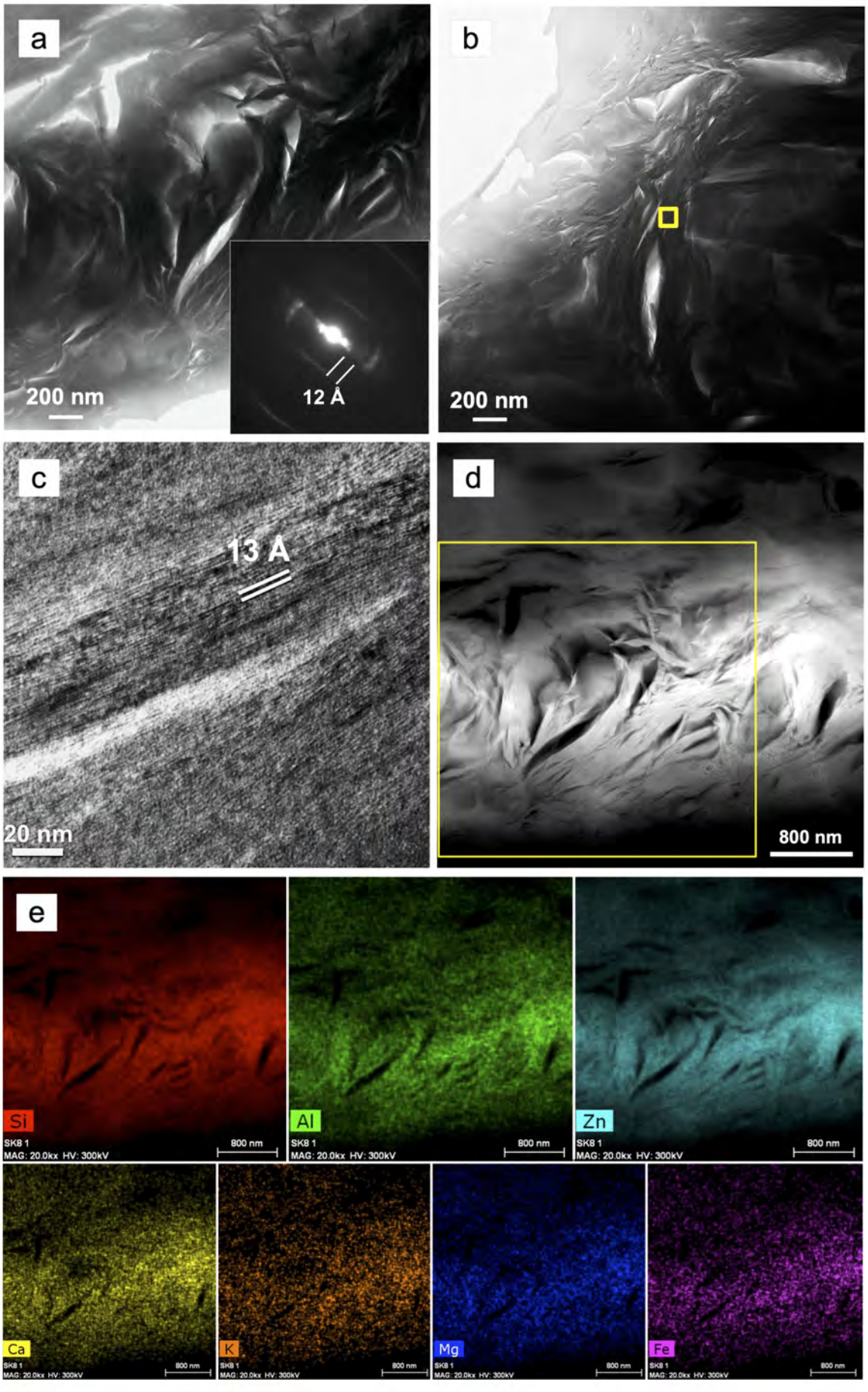

Fig. 8 Rev

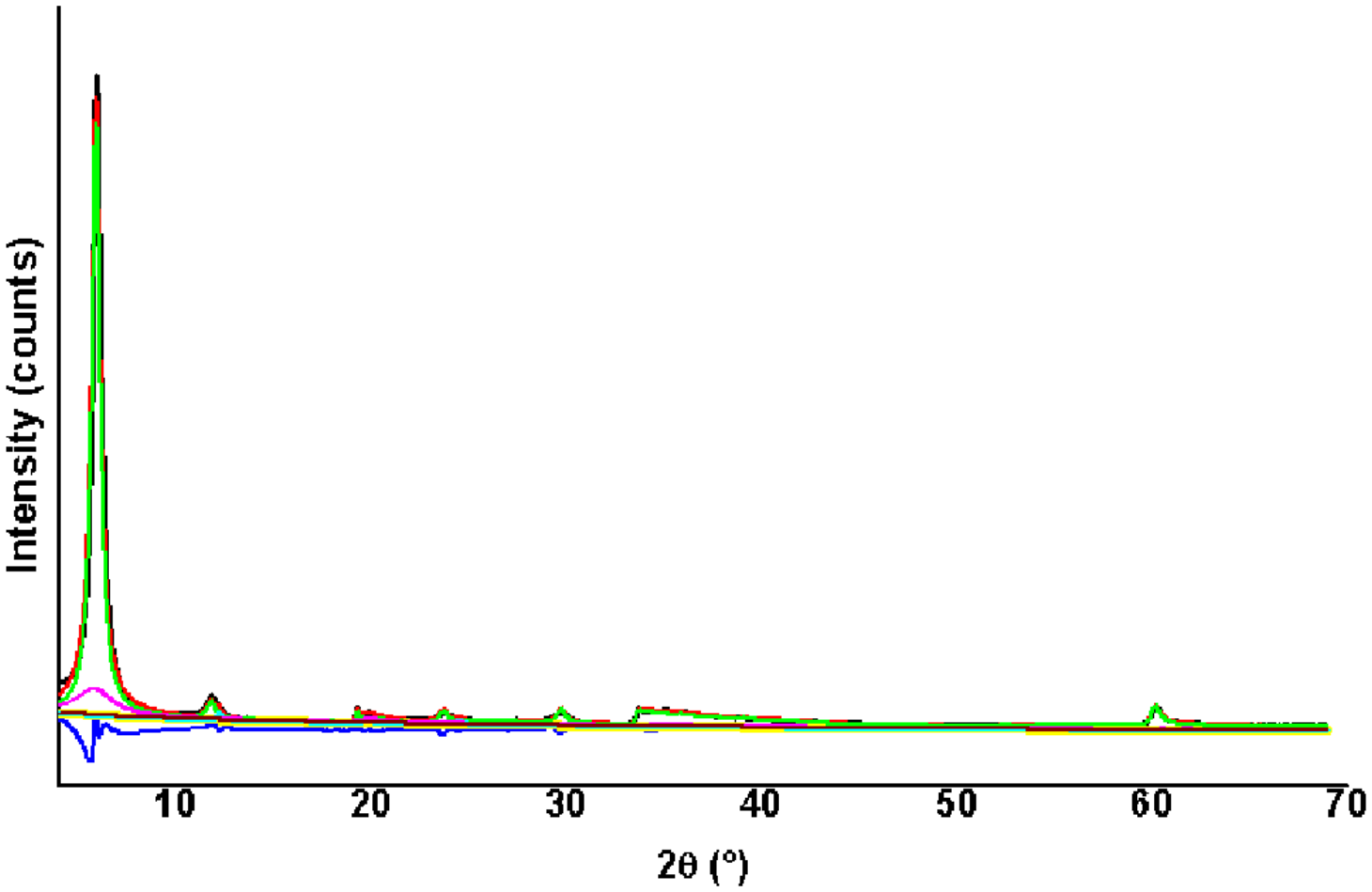

Fig. 9a Rev

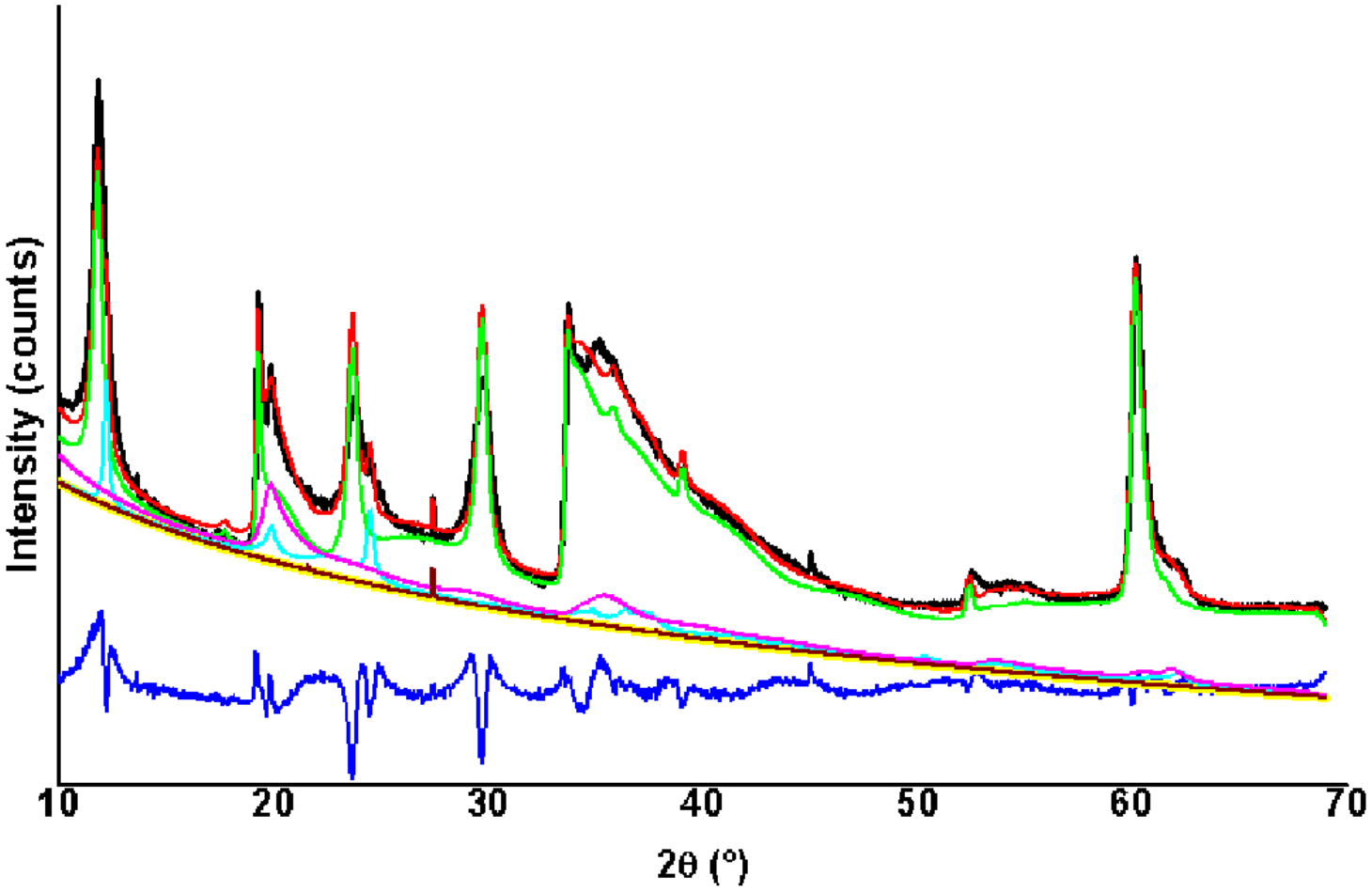

Fig. 9b Rev